

UNCLASSIFIED



Australian Government

Department of Defence

Defence Science and
Technology Organisation

Characterisation of High Grazing Angle X-band Sea-clutter Doppler Spectra

Luke Rosenberg

National Security and ISR Division

Defence Science and Technology Organisation

DSTO-RR-0397

ABSTRACT

Collection of radar sea-clutter for research purposes is typically performed from a clifftop looking out to sea as it is relatively simple and inexpensive. This constrains the radar look direction with respect to the wind and limits the grazing angle. To improve our understanding at high grazing angles in the range 15° to 45° , the DSTO's Ingara airborne X-band fully polarimetric radar has been used to collect 12 days worth of sea-clutter data. It has previously been shown that Walker's mean Doppler spectrum model is not suitable at these grazing angles and hence a new two component model is proposed which captures both the 'slow' Bragg component and the 'fast' non-Bragg component of the radar backscatter. A temporal decorrelation model is then presented which can be used to provide realistic performance prediction modelling.

APPROVED FOR PUBLIC RELEASE

UNCLASSIFIED

Published by

DSTO Defence Science and Technology Organisation

PO Box 1500

Edinburgh, South Australia 5111, Australia

Telephone: 1300 DEFENCE

Facsimile: (08) 7389 6567

© Commonwealth of Australia 2013

AR No. 015-704

August, 2013

APPROVED FOR PUBLIC RELEASE

Characterisation of High Grazing Angle X-band Sea-clutter Doppler Spectra

Executive Summary

Traditionally, maritime surveillance is conducted from low altitude platforms and hence with low grazing angles. This surveillance scenario has been well studied and relevant models have been developed. However, little data has been collected and analysed from the high grazing angles typically expected with the operation of high altitude airborne platforms. In August 2004 and July 2006, the Defence Science and Technology Organisation's (DSTO) Ingara X-band airborne radar collected fine resolution fully polarimetric data in the high grazing angle region $15^\circ - 45^\circ$. The data was collected in the ocean off the coasts of Port Lincoln and Darwin. The focus of this report is to characterise and model the mean Doppler spectrum over a range of sea conditions and geometries. Knowledge of the Doppler spectrum will increase our understanding of the underlying phenomenology and through its relationship with the temporal correlation, can aid with the development of target detection schemes and improve the realism of performance prediction modelling in the maritime environment.

Initial analysis considers a single Gaussian component as a model for the underlying Doppler spectrum. This is the chosen model used in many previous studies on sea-clutter and is useful as a baseline for the new model and comparing with results from the literature. Characterisation of the model parameters is performed over a range of wind speeds and azimuth and grazing angles. Results for the magnitude components show increasing magnitude with increasing grazing and a sinusoidal variation over azimuth with the largest value in the upwind direction. The centre point values show a peak for the horizontal transmit, horizontal receive (HH) channel when the grazing angle is small, which then decreases as the grazing increases. The spectral width is quite random over all azimuth and grazing angles, with the HH width more closely resembling the vertical transmit, vertical receive (VV) width at higher grazing angles. When considering the sea conditions, a good trend is observed with the mean width increasing as a function of wind speed and wave height.

A recent paper has characterised the Ingara sea-clutter to distinguish between different types of scattering [Rosenberg 2012*b*]. This study showed that the popular mean Doppler spectrum model proposed by Walker [2001*a*] is not suitable at these higher grazing angles and hence a new model is proposed. The new model contains two components representing the slow 'Bragg' and the fast 'non-Bragg' or 'sea-spike' scattering. The design of the model accounts for the reduced Brewster angle damping above 20° grazing and allows both polarisation channels to receive the fast component, albeit with a different magnitude.

For the dual polarised data set, there was a higher pulse repetition frequency (PRF) which resulted in a complete un-aliased Doppler spectrum with clear bi-modal components. This data was collected over a small range of grazing angles, but over all azimuth angles. The estimated magnitude results show the VV slow magnitude is greater than the HH channel. A sinusoidal variation is observed for both channels with the maxima in the upwind and downwind directions and the minima in the cross wind directions. For the fast magnitude, the HH return is always greater than VV indicating the presence of dominant fast components in the HH channel. Both model centre points vary sinusoidally around the upwind direction and there is no discernable trend for the width parameters over azimuth.

Fitting the two component model to the full-pol data sets is a more difficult estimation problem as the lower PRF results in aliasing of the sea-clutter Doppler spectra. The two component model however, still demonstrates an excellent fit to the data. Both the slow and fast magnitude components show a reasonable match with a sinusoidal variation over azimuth and with increasing magnitude as grazing increases. For the fast magnitudes, the relative levels are very similar with some sections where HH is greater than VV indicating where the non-Bragg scattering is more dominant. The model centre points demonstrate the sinusoidal variation with the slow component having a minimum in the upwind direction, while the fast component has a maximum. There is also a trend observed with decreasing value as the grazing increases which is more pronounced for the fast component. For the spreads, there is no discernable trend with the slow component, while there is a minor trend observed for the fast component with decreasing width as the grazing increases.

The temporal decorrelation is a metric commonly used in radar performance modelling for representing the level of temporal correlation present in the sea-clutter. The final contribution is to introduce a new model for this parameter as a function of wind speed and wave height.

Author

Dr. Luke Rosenberg*National Security and ISR Division*

Luke Rosenberg received his BE (Elec.) with honours from Adelaide University in 1999 and joined the DSTO in January 2000. Since this time he has completed both a masters degree in signal and information processing and a PhD in multichannel synthetic aperture radar through Adelaide University. He has worked at the DSTO as an RF engineer in the missile simulation centre, as a research scientist in the imaging radar systems group and now in the maritime radar group. Current research interests include radar and clutter modelling, radar imaging and detection theory.

THIS PAGE IS INTENTIONALLY BLANK

Contents

1	Introduction	1
2	Background	3
2.1	Composite surface model	3
2.2	Non-Bragg scattering	5
2.3	High grazing angle studies	5
2.4	Doppler line-shape models	7
3	Data processing and system model	9
3.1	Trials background	9
3.2	Radar description	10
3.3	Pre-processing	12
3.4	System model	13
3.5	Noise spectral density of the radar system	15
3.6	Aliasing	16
3.7	Formation of the Doppler spectrum	17
4	Sea-clutter analysis - single component model	19
4.1	Single component fit	19
4.2	Doppler spectrum	20
4.3	Single component variation over geometry - full-pol	22
4.4	Variation in sea conditions	26
5	Two component model	30
5.1	Two component model	30
5.2	Simulation	32
5.3	Fitting accuracy	33
6	Sea-clutter analysis - two component model	38
6.1	Dual-pol Doppler spectrum	38
6.2	Two component variation over azimuth - dual-pol	41
6.3	Co-pol Doppler spectrum	42
6.4	Two component variation over geometry - co-pol	43

7	Temporal correlation	47
7.1	Relationship between Doppler spectrum and temporal correlation	47
7.2	Temporal decorrelation model	49
8	Conclusion	51
	References	53

Appendices

A	Doppler spectrum convolution derivation	57
B	Convolution of two Gaussians	58

Figures

1	Circular spotlight mode collection geometry	10
2	Ingara pre-processing diagram	12
3	Azimuth normalised two-way beampattern	14
4	F35 noise estimate	15
5	F9 noise estimate	16
6	Aliasing example	17
7	Doppler spectrum comparison	18
8	Total number of range bins and observation times used for estimates in F35	18
9	Total number of range bins and observation times used for estimates in F9	18
10	Full-pol upwind range/Doppler sea-clutter image	21
11	Full-pol downwind range/Doppler sea-clutter image	21
12	Full-pol upwind mean Doppler spectrum with single component model	22
13	Full-pol downwind mean Doppler spectrum with single component model	22
14	Single component fit for F35, magnitude	23
15	Single component fit for F35, centre point	24
16	Single component fit for F35, width	24
17	F35 mean backscatter	24
18	Single component fit for F9, magnitude	25
19	Single component fit for F9, centre point	25
20	Single component fit for F9, width	25
21	F9 mean backscatter	26
22	Model magnitudes as a function of wind speed	27
23	Model width as a function of wave height / wave period	27
24	HH width as a function of wind speed and wave height	28
25	HV width as a function of wind speed and wave height	28
26	VV width as a function of wind speed and wave height	29
27	Verification block diagram	33
28	Example Doppler spectrum fits for dual-pol simulation	34
29	Example Doppler spectrum fits for full-pol simulation	34
30	Goodness of fit scatter plot, dual-pol	36
31	Goodness of fit scatter plot, full-pol	37

32	Dual-pol upwind range/Doppler sea-clutter image	39
33	Dual-pol downwind range/Doppler sea-clutter image	39
34	Dual-pol upwind mean Doppler spectrum	40
35	Dual-pol downwind mean Doppler spectrum	40
36	Dual-pol model magnitudes	41
37	Dual-pol model centre points and widths	41
38	Co-pol upwind mean Doppler spectrum with two component model	42
39	Co-pol downwind mean Doppler spectrum with two component model	42
40	Two component model fit for F35, slow magnitude	44
41	Two component model fit for F35, fast magnitude	44
42	Two component model fit for F35, centre point	44
43	Two component model fit for F35, width	45
44	Two component model for F9, slow magnitude	45
45	Two component model fit for F9, fast magnitude	45
46	Two component model fit for F9, centre point	46
47	Two component model fit for F9, width	46
48	Autocorrelation example	47
49	Temporal decorrelation time for F35 using single component model	48
50	Temporal decorrelation time for F35 using two component model	48
51	Temporal decorrelation time for F9 using single component model	48
52	Temporal decorrelation time for F9 using two component model	49
53	HH mean temporal decorrelation as a function of wind speed and wave height . . .	50
54	VV mean temporal decorrelation as a function of wind speed and wave height . . .	50

Tables

1	Wind and wave ground truth	11
2	Nominal geometric parameters for circular spotlight-mode collections	11
3	Standard radar operating parameters for ocean backscatter collections	11
4	Bounds used for the single component fit	20
5	Full-pol single component model parameters	20
6	Sea variation width model coefficients	27
7	Bounds for the two component model fit	31
8	Relevant simulation parameters	32
9	Model parameters and estimation errors for simulation example	33
10	Range of model parameters used in verification	35
11	Dual-pol parameter deviation error and correlation values	36
12	Full-pol parameter deviation error and correlation values	37
13	Dual-pol two component model parameters	40
14	Co-pol two component model parameters	43
15	Temporal decorrelation model parameters	49

THIS PAGE IS INTENTIONALLY BLANK

1 Introduction

An active area of research at the Defence Science and Technology Organisation (DSTO) is to understand the characteristics of sea-clutter as seen by an X-band radar, specifically the mean backscatter, amplitude statistics and the Doppler spectrum, [Rosenberg 2012*b*, Crisp et al. 2008, Dong 2006, Rosenberg, Crisp & Stacy 2010, Rosenberg & Stacy 2008, Rosenberg, Crisp & Stacy 2008]. The two papers on the Doppler spectrum by Rosenberg & Stacy [2008] and Rosenberg, Crisp & Stacy [2008] utilised Walker's model [Walker 2001*a*] with good results. There was a question raised however about the suitability of the model for grazing angles above 20° where Brewster angle damping is not present and there may be both persistent and discrete 'sea-spikes' present in both horizontal transmit, horizontal receive (HH) and vertical transmit, vertical receive (VV) polarisation channels. To answer this question, a recent paper characterised the Ingara sea-clutter to distinguish between different types of scattering [Rosenberg 2012*b*]. This study showed that Walker's model is not suitable at high grazing angles and hence a new two component model is proposed in this report which captures both the slow 'Bragg' and the fast 'non-Bragg' or sea-spike scattering for each polarisation channel. Knowledge of the mean Doppler spectrum enables the temporal correlation of the sea-clutter to be measured and then used for simulation and radar performance analysis. Recent analysis [Rosenberg 2012*a*] has shown that if the temporal correlation is not accounted for correctly, the required signal to interference ratio for a given probability of detection will be incorrect by several dB, resulting in over-estimated performance.

In August 2004 and July 2006, the DSTO Ingara X-band airborne radar [Stacy et al. 2003], collected fine resolution dual and fully polarimetric data off the coasts of Port Lincoln and Darwin. The data analysed here is from the spotlight mode collected from a circular flight path around the scene of interest covering the grazing angle region 15° to 45° . For the dual polarised (dual-pol) mode, the radar transmits with either a horizontal or vertical polarisation and then receives both polarisations. In the fully polarimetric (full-pol) mode, the effective pulse repetition frequency (PRF) is halved as the radar alternates between transmitting horizontal and vertical polarisations, while receiving both. The result is that only the dual-pol mode is able to measure the entire un-aliased sea-clutter Doppler spectra, while the full-pol mode suffers from aliasing. This causes the edges of the spectrum to be raised as the aliased components wrap into the sampled frequencies. In addition to this, the Doppler spectra measured by a moving airborne platform is widened by the aspect dependent Doppler spread due to the radar beam footprint (azimuth antenna beampattern) with the result being a convolution of the Doppler spectra with the azimuth beampattern. Rather than trying to deconvolve the beampattern from the received data, a 'spread' spectrum model is formed using the 'underlying' spectrum convolved with the azimuth beampattern. This model is then fitted to the data to determine the model parameters with the best fit. The estimated parameters are then used to characterise the underlying model over a range of wind speeds and azimuth and grazing angles. The main contribution from this work is the justification of the two component model and characterisation of the high grazing angle Ingara data.

This report is divided up into a number of sections. Section 2 describes the main results from the literature relevant to modelling high grazing angle sea-clutter and the line-shape models which have been used to represent the mean Doppler spectrum. Section 3 then provides relevant background on the Ingara radar, details on the sea-clutter trials, the system model and formation of the Doppler spectrum. In Section 4, a single Gaussian component is used to model the Doppler spectrum. The analysis includes variation with azimuth and grazing angle as well as wind speed and wave height.

The second part of the report considers a two component model for describing the Doppler spectrum. Section 5 describes this model and the verification which was performed with simulated data. This is followed by Section 6 which uses this model to analyse both dual and full-pol data sets. The final Section 7 then presents a model for the temporal decorrelation as a function of both the wind speed and wave height.

2 Background

The ocean surface is a highly complex dynamical system and relating Doppler spectra to surface conditions is a difficult problem. There are a number of textbooks that focus on aspects of sea-clutter [Skolnik 2008, Nathanson, Reilly & Cohen 1991, Long 2001, Ward, Tough & Watts 2006]. The first two by Skolnik [2008] and Nathanson, Reilly & Cohen [1991] summarise the early work from the 1960s and 1970s. However, that work is of limited use for this study, since much of it treated the Doppler spectra as a whole, with only the mean Doppler shift and the total bandwidth being considered. Also, they focus predominantly at low grazing angles making comparison with our higher grazing angle results difficult. Long [2001], as well as discussing this early work with detailed notes on the literature, goes on to the more recent work, such as [Lee et al. 1995b] which considers higher grazing angles. Ward, Tough & Watts [2006] is focussed mainly on low grazing angle sea-clutter but does discuss a number of Doppler line-shape models in detail. Apart from a figure showing that the trend in mean Doppler shift against azimuth is sinusoidal, the book has few details on how the spectrum varies with other geometric and wind/wave conditions.

The first part of this section presents a summary of the key milestones in understanding the scattering present in sea-clutter backscatter. Section 2.1 describes the early years, where the focus was on matching experimental data with a combination of electromagnetic and rough surface scattering theory. The ‘composite surface model’ was originally proposed to describe the wind and wave interaction in terms of Bragg scattering theory. Further research then led to hydrodynamic models which were used to explain the physical nature of the waves and showed a good match with the existing theory. However, as more experimental data was collected, it was found that larger wind speeds caused waves which travelled at speeds faster than was predicted by the Bragg theory. Section 2.2 then describes the history of non-Bragg scattering with descriptions of the ubiquitous ‘sea-spike’. This leads to Section 2.3 which describes the results from a number of high grazing angle sea-clutter studies and Section 2.4 which describes the line-shape models that have been developed to model the mean Doppler spectrum.

2.1 Composite surface model

The perturbation theory for electromagnetic scattering was developed by Rice [1951] and later applied by Peake [1959] to compute radar cross section. Wright [1966] then extended this theory to water and classified it as a ‘slightly rough’ surface. He showed that the scattering elements of primary importance for grazing angles much less than 90° are capillary or short-gravity waves which satisfy the Bragg equation for a given wavelength and direction of the incidence field. This is the definition for the Bragg water-wave propagation number defined in the spatial frequency domain as $k_w = 2k_0 \cos \theta$, where $k_0 = 2\pi/\lambda$ is the microwave wave-number with λ representing the radar wavelength and θ is the grazing or depression angle.

An early study by Wright [1968] suggested that the radar backscatter can be interpreted in terms of wind and wave components. Wright found that the first order Bragg scattering condition can be used to explain data from small amplitude, mechanically generated water waves where the radar backscatter is proportional to the square of the water wave amplitude with the water wave propagation constant maximum when $k = k_w$. This first order approximation however is only valid when the fetch and wind speeds are very small and consequently, the backscatter return from the waves are small in amplitude. To extend this theory, two scale composite surface theories

were proposed which divide the rough surface into large and small-scale components. The large scale component is treated by geometric or physical optics and the small-scale component by the existing perturbation theory. A number of authors have looked at different variations of this including [Wright 1968, Guinard & Daley 1970, Valenzuela, Laing & Daley 1971, Bass et al. 1968, Hasselmann & Schieler 1970].

A different approach to explain the radar backscatter was adopted by Valenzuela & Laing [1970] who used hydrodynamic models to justify the two-scale composite model. This provides a more physical description of the sea surface where large swells are present with short gravity and capillary waves superimposed. Effects of the sea and swell are included by considering changes in scattering caused by the ‘tilting’ of the short gravity and capillary waves by the sea and swell. Studies using this theory focused on the spectral width and location of the Doppler shift, [Hicks et al. 1960, Pidgeon 1968, Valenzuela & Laing 1970]. Hicks et al. [1960] studied data at X-band with low grazing angles and found for some experimental conditions that the Doppler bandwidth was proportional to the wind speed and also to the ratio of the significant wave height and wave period. Bass et al. [1968] later gave a theoretical basis for the width of the Doppler spectrum being proportional to the ratio of wave height to wave period.

Experimental data with higher wind speeds then started to reveal more than one significant component to the Doppler spectrum. For low sea-states, Hicks et al. [1960] found that the spectrum had a Gaussian shape which broadened as the wind speed increased and become asymmetrical. Wright [1968] and later Duncan, Keller & Wright [1974] also found a second component which could not easily be explained using the composite scattering theory. This was found at low grazing angles particularly with the horizontal polarisation. Other authors, [Pidgeon 1968, Valenzuela & Laing 1970, Rozenberg, Quigley & Melville 1996] found the Doppler spectra shifted to a much higher level for the HH channel than the VV channel which is contrary to the composite surface theory which states that the Doppler shifts should be identical, aside from a small difference due to power-frequency correlations as noted by Hasselmann & Schieler [1970]. Also, the above theory implies that the instantaneous polarisation ratio (HH/VV) should be bounded by an upper limit of 0 dB, which was found to not always hold, [Lee et al. 1995a].

Nevertheless, a number of authors have used or extended the composite surface model to account for these changes. Duncan, Keller & Wright [1974] used a wave tank to vary the fetch and proposed that at lower grazing angles, there are both free and bound capillary waves. At high wind speeds, the bound waves are then tilted by the dominant wave and travel at the same speed. [Kalmykov & Pustovoytenko 1976, Lewis & Olin 1980] propose that ‘wedge scattering’ is present at low grazing angles where surface elements are present with a small radius of curvature relative to the radar wavelength. This mechanism is meant to explain the larger backscatter return when large scale waves are near breaking. Lyzenga, Maffett & Shuchman [1983] then showed how to combine the wedge scattering theory with the composite surface model. Plant [1997] proposes that in the low grazing region, wind causes intermediate waves to travel on the underlying swell which are steep enough that some of the short capillary waves are bound to it. Hence, they travel at a faster speed causing a larger Doppler shift.

These theories may work in many situations, but clearly it does not capture all the observed sea behaviour. What then is the mechanism which gives rise to this observed data?

2.2 Non-Bragg scattering

Over the past years, a number of authors have proposed different theories to explain the sea dynamics due to non-Bragg scattering, [Duncan, Keller & Wright 1974, Jessup, Keller & Melville 1990, Jessup, Melville & Keller 1991*a*, Werle 1995, Lee et al. 1995*a*, Keller, Gotwols & Chapman 2002, Melief et al. 2006]. These are primarily concerned with analysis of breaking waves and understanding the main components of the associated radar response. Non-Bragg scattering is commonly represented as a single component and referred to as ‘sea-spikes’. A common definition of a sea-spike is a radar return which has a large Doppler component with a wide bandwidth, strong backscatter power as well as a HH return that is equal to or greater than the VV return. Lee et al. [1995*a*] summarises three possibilities to explain the phenomena which contribute to non-Bragg scattering:

- There is a wave which is about to break and has a much longer wavelength than the Bragg resonant wave.
- There is a breaking wave which has a long wavelength and large specular return.
- There is an attenuation in the VV channel due to Brewster angle damping and the HH channel is affected by multipath scattering and shadowing of the wave troughs by large crests.

Alternatively, Long [2001] has distinguished sea-spikes by their duration, with some lasting for a short time before fading rapidly and others persisting for 1-2 seconds. These second type are what are commonly mistaken for targets as they may exhibit many of the same characteristics including polarisation independence.

For the third point, the Brewster angle is the point at which the incident signal completely passes through the sea-surface with no reflection and depends on the ratio of the refractive indices of the two media. This has been calculated to be approximately 7° grazing at X-band, [Walker 2001*a*] and its effects observed in data collected as high as 20°, [Trizna 1997]. The effect of Brewster angle damping is that more of the incident signal will penetrate the water from vertically polarised signals than from horizontal ones, [Pidgeon 1968]. The result for the backscattered signal (in the power domain) is a polarisation ratio of 12 dB or greater. More information on Brewster angle damping can be found in [Pidgeon 1968, Sletten, Trizna & Hansen 1996, Trizna 1997].

There have also been a number of studies looking at methods for distinguishing between Bragg scattering and sea-spikes [Jessup, Melville & Keller 1991*a*, Keller, Gotwols & Chapman 2002, Greco, Stinco & Gini 2010, Rosenberg 2012*b*]. These are based on discriminating between different aspects of the radar backscatter such as the magnitude, Doppler spectral width and the interval between sea-spikes.

2.3 High grazing angle studies

Sea-clutter studies have been performed from a number of different platforms and locations including cliff tops, observation platforms, boats, planes and wave tanks. The following descriptions

outline the key points relevant to the Doppler spectrum in the high grazing angle region above 20° with variation of wind direction, wind speed and polarisation.

The most comprehensive study on X-band scattering is by Lee et al. [1995a] who looks at the grazing angle range of 10° to 70° using a coherent scatterometer mounted on the bow of a boat. They found the following:

- In the upwind direction, as the grazing angle increases, the mean Doppler velocity reduces, approximately in proportion to $\cos \theta$. This was also observed by Nathanson, Reilly & Cohen [1991].
- The higher velocity (Doppler) peak observed with HH polarization reduces relative to the peak for VV polarisation, so that at higher grazing angles, typically $\theta > 50^\circ$, the velocities are approximately equal with very similar spectral shapes.
- At upwind as the grazing angle decreases, the HH Doppler peak separates from the VV peak by shifting to a higher frequency.
- At upwind (25° grazing), the non-Bragg spectral peak for the HH polarisation is a few dB larger than the Bragg peak.
- At upwind, by removing the Bragg component with a high pass filter, sea-spikes were found at all grazing angles.
- At crosswind, the non-Bragg component is much smaller than the Bragg component and was not observed above 25° grazing. As a result, both the HH and VV spectra appeared the same.
- The decorrelation time determined from the autocorrelation function of the HH and VV spectrums increased with grazing angle.

Another relevant two part study is by [Jessup, Melville & Keller 1991a, Jessup, Melville & Keller 1991b] who used a Ku band scatterometer on an observation platform based 26 m above the Chesapeake Bay. The following observations were made:

- Waves which produced whitecaps were not necessarily associated with a large spike in the radar backscatter. However, many broken waves had an associated spike in the radar backscatter.
- Sea spikes associated with breaking waves tended to be accompanied by an increased mean Doppler frequency and broadening of the Doppler bandwidth.

There have been a large number of wave tank studies, but only a few looking at the high grazing angle region, [Duncan, Keller & Wright 1974, Kwok & Lake 1983, Melville, Rozenberg & Quigley 1995, Lee et al. 1996, Rozenberg et al. 1997, Lamont-Smith 2004]. Using a wave tank allows a much more controlled environment with respect to the wind direction, speed and waves. They are however unable to fully replicate the long scale swells that are present in the ocean. The key points from these studies include:

- The Doppler bandwidth increases with increasing fetch, [Duncan, Keller & Wright 1974].

- The non-Bragg spectral peak becomes stronger as the wind speed increases, [Kwoh & Lake 1983].
- The non-Bragg returns do not always correspond to wave breaking, [Lee et al. 1996].
- Rozenberg et al. [1997] observed that the effect of long waves/swell can change a significant number of non-Bragg scatterers in the upwind HH backscatter to Bragg scatterers, while for the VV backscatter, the reverse is true at high wind speed and a significant number of Bragg scatterers become non-Bragg. Interestingly, this effect did not appear in the downwind direction.
- Lamont-Smith [2004] found that the non-Bragg component showed a linear dependence between both the HH and VV Doppler spectral peaks and the grazing angle. This was consistent (albeit with a different slope) over different wind speeds and radar frequencies.

There are only a few relevant airborne studies concerned with the Doppler spectrum [Valenzuela, Laing & Daley 1971, Ritchie, Woodbridge & Stove 2010]. For the former study, Valenzuela et al. looked at the polarisation dependence of HH and VV over 10° to 30° grazing and discuss how the azimuth beam pattern will spread the observed scatterer velocities. They claim this effect is minimal and focus their study primarily on the spectral width of the Doppler spectrum, where they found:

- It decreases with increasing radar frequency.
- It is greatest upwind and smallest in the downwind.
- It increases with wave height.
- For the vertical polarisation, it is almost independent of grazing angle, while for the horizontal polarisation, the width decreases to the vertical level as the grazing angle increases.

2.4 Doppler line-shape models

In the past, Hicks et al. [1960] suggested that the ‘core’ Bragg component has a Doppler line-shape that is nearly Gaussian and can be used to represent the Doppler spectrum. There are three relevant models in the literature which use this as a starting point, albeit they have only considered the low grazing region and are based on data collected either from a cliff top or wave tank.

The first model considered is by [Lee et al. 1995b, Lee et al. 1998] and comprises two components, a Gaussian for the Bragg scatterers and a Lorentzian and/or Voigtian for the non-Bragg component. The model describes the Doppler spectrum with a good degree of accuracy, but is complicated to interpret and hence relate to the scattering phenomenology. A similar model was used by Lamont-Smith [2004] who looked at the effect of varying the grazing angle with data collected from both a large wave tank and from a cliff top. His model uses a single Gaussian to represent the ‘slow’ Doppler component which dominates the VV channel, and two Gaussian components to represent the slow and ‘fast’ components in the HH channel. This also corresponds with later observations by Melville, Rozenberg & Quigley [1995] who found that the non-Bragg term was virtually absent in their VV channel data.

Many authors investigating sea-spikes observed that there is a degree of polarisation independence in the non-Bragg component when looking at sea-clutter backscatter, [Duncan, Keller & Wright 1974, Werle 1995, Walker 2000]. Jessup, Melville & Keller [1991a] observed that as the grazing angle increased, the polarisation ratio (HH/VV) which is typically less than one, now approached unity. As a result, the model presented by [Walker 2000, Walker 2001a, Walker 2001b] uses a combination of three Gaussian components to describe the Doppler spectrum. These are referred to as 'Bragg', 'whitecap' and 'spike'. In this model, the non-Bragg scatterers are explained by two components. The whitecaps are associated with the polarisation independent returns from the breaking waves. They are incoherent and occur for seconds. Spikes however, are defined as coherent scatterers which capture the specular returns and last for a small fraction of a second with the HH magnitude much greater than VV. This model has been applied to our data in the past, [Rosenberg & Stacy 2008, Rosenberg, Crisp & Stacy 2008] with good results. There is a question however about whether the third spike component is present in the VV channel when the grazing angle is above 20° and Brewster angle damping is not present.

This led to the work by Rosenberg [2012b] who used a threshold to isolate the non-Bragg scatterers in the range/time domain. An image processing algorithm was then used to isolate discrete and persistent scatterers and test whether Walker's mean Doppler spectrum model is valid in the grazing angle region 15°-45°. The results found that the whitecaps were spread quite evenly in grazing and azimuth for the HH channel with more detections in the crosswind directions for the HV and VV channels. While there were many common peaks in both the HH and VV channels, there were however, a lot of detections present in HH but not in VV. There were also many discrete scatterers detected in the VV channel. This indicates that Walker's three channel model is not totally valid at high grazing angles and a different model is therefore required to represent the mean Doppler spectrum.

3 Data processing and system model

This section provides a summary of the sea-clutter data which has been collected and the processing which occurs prior to the analysis and model fitting. Background to the two sea-clutter trials is presented in Section 3.1 followed by a brief description of the Ingara radar in Section 3.2. Section 3.3 then describes the pre-processing steps for removing the sensor specific effects from the raw data and other artifacts which can bias the statistics. A description of the system model is then presented in Section 3.4 followed by descriptions of how the thermal noise power of the radar system is determined in Section 3.5 and how the aliasing is accounted for in Section 3.6. The final Section 3.7 shows how the collected data is used to form the mean Doppler spectrum.

3.1 Trials background

The trial data was obtained with Ingara on two separate occasions and two distinctly different regions. The first ‘sea-clutter’ trial was conducted in 2004 (SCT04) in the southern ocean approximately 100 km south of Port Lincoln, South Australia [Crisp, Stacy & Goh 2006]. The site chosen was at the edge of the South Australian continental shelf where there was little chance of shallow water affecting the wave field. During the trial, ocean backscatter was collected for a range of different geometries on eight separate days with different ocean conditions. The second ‘maritime surveillance’ trial was conducted in 2006 (MAST06) in littoral and open sea environments near Darwin in the Northern Territory. Again, data was collected for a range of different geometries and ocean conditions. In this trial, a total of four days data were collected: two of the days were in the littoral zone approximately 25 km north of Darwin and the other two days were in the open ocean approximately 200 km west of Darwin.

During the ocean backscatter collections, Ingara was operated in the circular spotlight-mode as shown in Figure 1. In this mode, the aircraft flies a circular orbit in an anti-clockwise direction (as seen from above) around a nominated point of interest, while the radar beam is continuously directed toward this point. Radar echo data is continuously collected during the full 360° orbit, with the instantaneous PRF appropriately adjusted to maintain a constant spatial pulse separation between pulse transmission positions. Once collected, the echo data may be processed either immediately (in real-time) or subsequently (off-line) to produce either range-compressed profiles or spotlight images of the scene at various azimuth angles. Further, owing to the continuous nature of the data collection, the images can be formed at any desired azimuth look direction. Each collection of data in this mode is referred to as a ‘run’ and there may be several complete orbits in a single run.

In order to examine the effect of grazing angle on ocean backscatter, runs were made with different altitude and orbit diameters. Owing to the finite beam width of the radar, its footprint on the ocean surface has a significant range extent. This means that the grazing angle varied across the footprint. It follows that, with appropriate range compression and data processing, the variation in backscatter with grazing angle across the range extent of the radar beam footprint can be measured. For both the SCT04 and MAST06 trials, backscatter measurements for most grazing angles in the range from 15° to 45° could be extracted from the data.

Note that the aircraft speed was approximately 100 m/s and so a 1.5 NM orbit took approximately 3 minutes while a 1.9 NM orbit took 3.5 to 4 minutes. The total collection across all grazing

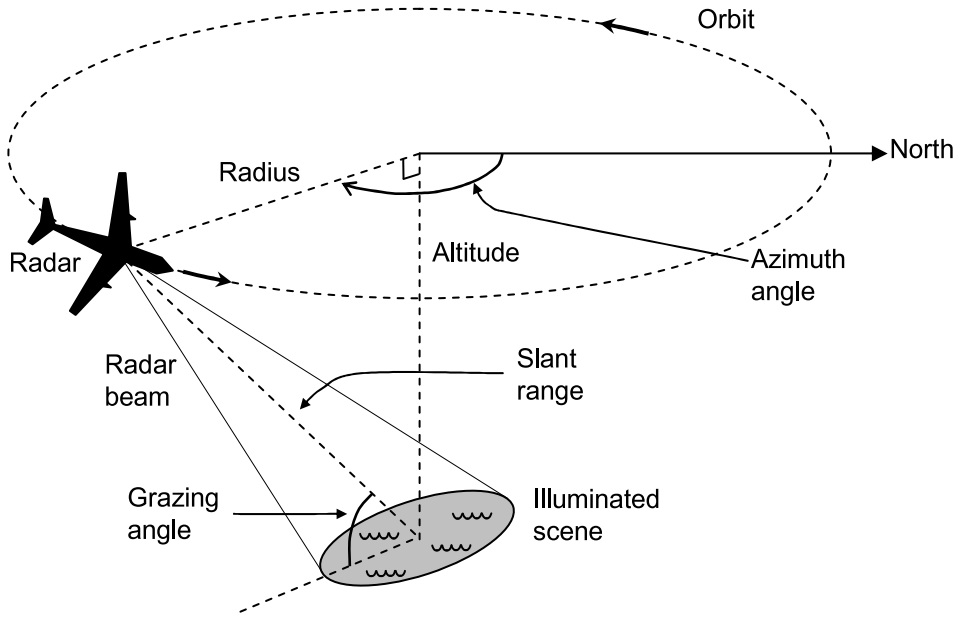


Figure 1: Circular spotlight mode collection geometry

angles took approximately 90 minutes. It is reasonable to assume that over such short time intervals, the ocean surface conditions are relatively unchanged and that mean backscatter variations are mostly due to the changing imaging geometry rather than changing ocean conditions. Nevertheless, it is possible that wind gusts and changes of wind strength and direction may have effected the measurements. Table 1 shows the wind and wave ground truth for the data used in this report. The majority of collections on these days used the full-pol mode with a PRF of approximately 300 Hz, with a small number of dual-pol collects with a PRF of close to 600 Hz. For the full-pol model analysis in the following sections, F35 and F9 are used as example data sets for each trial. The dual-pol data set was collected on flight F9.

Finally, using the geometry in Figure 1, the azimuth resolution can be calculated approximately by $R\Delta\psi$, where R is the slant range distance between the radar platform and the patch of ocean and $\Delta\psi$ is the two-way azimuth antenna 3 dB beamwidth. Table 2 shows the geometry for collections at a range of grazing angles and slant ranges for a beamwidth of 1° . Over these nominal parameters, the average azimuth resolution is 62.7 m. However since each collection spans a range of grazing angles, the actual azimuth resolution will always differ slightly. For the examples presented in this report, the upwind direction (wind towards the radar) is rotated to 0° with the downwind direction at -180° and the crosswind directions at $\pm 90^\circ$. Any regions with poor or missing data are shown with ‘hashed’ diagonal stripes.

3.2 Radar description

The DSTO Ingara system is an airborne multi-mode X-band imaging radar system. It operates with a centre frequency of 10.1 GHz and supports a 600 MHz bandwidth for fine resolution in a spotlight mode. The sea-clutter trials however used a bandwidth of 200 MHz to achieve a larger swath width. The radar is fully polarimetric and utilises a dual linear polarised antenna developed by the Australian CSIRO for both transmitting and receiving [Parfitt & Nikolic 2001].

Table 1: Wind and wave ground truth. Directions are “from” not “to”

Trial	Flight	Date	Wind		Wave		
			Speed (m/s)	Direction (°)	Height (m)	Direction (°)	Period (s)
SCT04	F33	9/8/04	10.2	248	4.9	220	12.3
SCT04	F34	10/8/04	7.9	248	3.5	205	11.8
SCT04	F35	11/8/04	10.3	315	2.6	210	10.4
SCT04	F36	12/8/04	13.6	0	3.2	293	8.8
SCT04	F37	16/8/04	9.3	68	2.5	169	9.7
SCT04	F39	20/8/04	9.5	315	3.0	234	11.4
SCT04	F40	24/8/04	13.2	22	3.8	254	12.2
SCT04	F42	27/8/04	8.5	0	4.3	243	12.5
MAST06	F2	17/5/06	8.5	115	0.62	112	3.1
MAST06	F4	19/5/06	3.6	66	0.25	35	2.6
MAST06	F8	23/5/06	3.5	83	0.41	46	4.0
MAST06	F9	24/5/06	10.2	124	1.21	128	4.6

Table 2: Nominal geometric parameters for circular spotlight-mode collections

Grazing angle (°)	Altitude (m)	Radius (NM / m)	Slant range (m)	Azimuth res. (m)
15	932	1.9 / 3519	3643	63.54
20	1353	1.8 / 3334	3548	62.80
25	1522	1.8 / 3334	3679	63.97
30	1711	1.6 / 2963	3421	59.72
35	2073	1.6 / 2963	3617	63.11
40	2314	1.5 / 2778	3626	63.10

In fully polarimetric collections, the system is operated at half the PRF with the polarisation being switched to alternately transmit horizontal and vertical, while receiving both simultaneously. A more detailed description of the system may be found in [Stacy et al. 2003]. The standard radar operating parameters used during the sea-clutter collections are shown in Table 3.

Table 3: Standard radar operating parameters for ocean backscatter collections

Parameter	Value
Frequency	10.1 GHz
Transmitted bandwidth	200 MHz
Range resolution	0.75 m
Pulse length	20 μ s
Peak transmit power	1 kW
3 dB beamwidth - azimuth / elevation	1°/13°
Specified pulse separation	0.15 m
Full-pol. pulse separation	0.30 m

3.3 Pre-processing

Before the data was analysed, a number of pre-processing steps were applied. Range processing occurs in hardware as a stretch process. The sampled signal was then processed to first remove bandpass filter modulations and adjusted for motion compensation using both the inertial navigation unit and the global positioning system onboard the radar platform. The next steps included a radiometric correction due to changes in grazing angle, removal of the elevation beampattern and polarimetric calibration using the procedure described in [Quegan 1994]¹. Since the platform motion was not perfectly compensated and the antenna was not pointing directly broadside, the absolute Doppler origin was unknown and there was an extra Doppler shift present in the received signal. Therefore, to ensure the correct separation between channels, the total Doppler centroid was estimated using the wavelength diversity algorithm [Bamler & Runge 1991] and the VV channel was centred at the Doppler origin. The HH and HV channels were then shifted by the difference between HH and VV and HV and VV respectively. Note that due to a problem with the cross-pol calibration, the HV Doppler spectrum does not always lie between the HH and VV channels and consequently, only the HH and VV channels are used for constructing the new Doppler spectrum model.

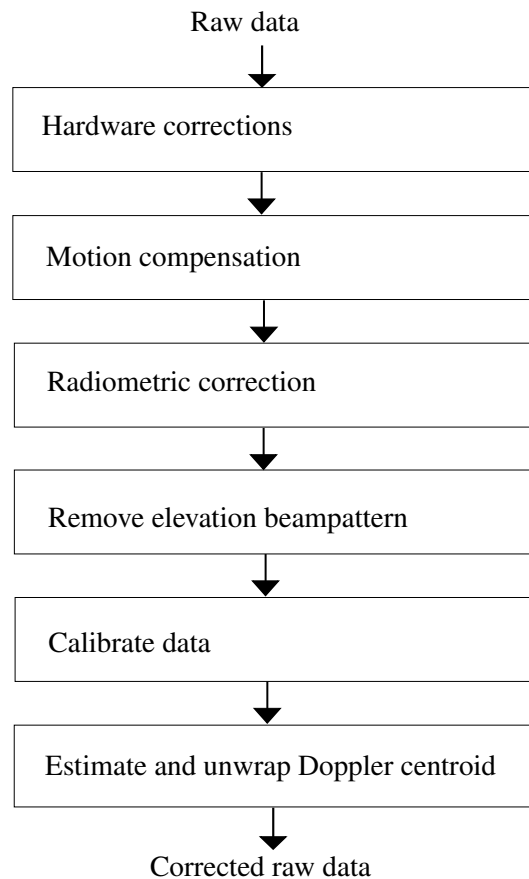


Figure 2: Ingara pre-processing diagram

¹Note that the cross talk term was assumed to be negligible for the dual-pol data.

3.4 System model

Determining an appropriate Doppler spectral model of the surface backscatter requires careful consideration of the measurement process. In particular, the Doppler spectra of the scene as measured by a moving airborne platform is widened by the Doppler spread due to the radar beam footprint (antenna azimuth beampattern). This occurs since the antenna has a finite azimuth beam width, which ‘observes’ each sea-clutter return over a range of different Doppler frequencies. The result is a convolution of the sea surface spectra with the azimuth beampattern. To relate the beampattern to the Doppler spectrum, consider the circular motion of an aircraft around a patch of ocean. At the centre of rotation, the slant-range and azimuth are defined as $(x(t), y(t))$ and the time evolution is determined by the slant range at the centre of the patch, R and angular velocity, ω_p

$$x(t) = R \cos(\omega_p t), \quad (1)$$

$$y(t) = R \sin(\omega_p t) \quad (2)$$

where the angular and linear platform velocities are related by $\omega_p = v_p/R$. Now consider a patch of ocean at distance (x_1, y_1) from the middle of the swath. The radial distance to the aircraft is

$$r(t|x_1, y_1) = \sqrt{(R \cos(\omega_p t) - x_1)^2 + (R \sin(\omega_p t) - y_1)^2} \quad (3)$$

and hence the time varying Doppler shift can be determined by

$$f(t|x_1, y_1) = -\frac{2}{\lambda} \frac{\partial r(t|x_1, y_1)}{\partial t} \quad (4)$$

$$= \frac{2v_p}{\lambda r(t|x_1, y_1)} [y_1 \cos(\omega_p t) - x_1 \sin(\omega_p t)]. \quad (5)$$

Figure 3 shows the azimuth beampattern in the slant plane for a single range bin and for the three polarisation channels. The 3 dB beamwidth is measured as approximately 1° for each of the three polarisation channels and the peak sidelobes are 35.0 dB, 31.7 dB and 27.8 dB below the mainlobe for the HH, HV and VV channels respectively. There are also slight offsets from the centre frequency for each channel. This is the reason for the antenna pointing errors which were mentioned above. To ensure that the relative offsets between the channels are maintained, the beampattern for the VV channel is centred, while the other two channels are shifted by the same amount. The offset for the HH and HV channels are then 5.31 and 2.64 Hz respectively. Consider an example with 100 m/s radar platform velocity, 0.03 m radar wavelength, 2 s observation time a slant range of 3000 m which corresponds to a 50 m azimuth resolution. Along the centre of the patch, $(x_1, y_1) = (0, 25)$ and the 3 dB Doppler width is calculated as 111 Hz. In general, the 3 dB width must be determined for each given observation time and slant range or grazing angle according to Equation 5.

Rather than trying to deconvolve the beampattern from the received data, a system model is now presented which explicitly includes the convolution of the antenna beampattern with the received data. For this model to hold however, the observation time must be carefully chosen to make sure that the Doppler frequency in Equation 5 has constant bin spacing and is approximately linear. This requires careful selection of the data region as discussed in Section 3.7. In the circular spotlight data collection mode, each scatterer can be modelled with position (x_l, y_m) and velocity (v_{x_l}, v_{y_m}) components with the indices (l, m) relating the position index in the slant-range and

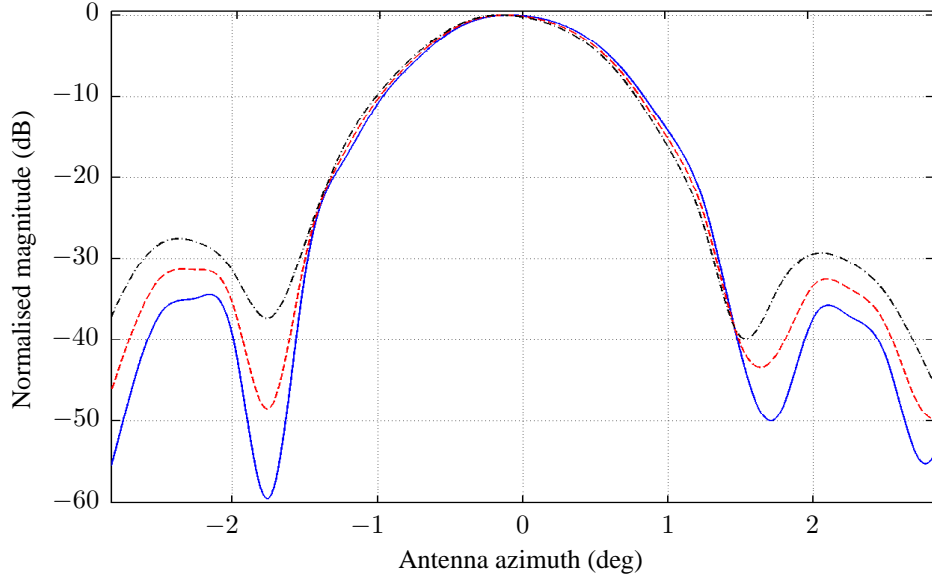


Figure 3: Azimuth normalised two-way beampattern, (—) HH, (---) HV, (· · ·) VV

azimuth directions. The total clutter return measured by the radar in the spatial frequency (k_x, k_y) domain post range processing and after motion compensation can be written as

$$X(k_x, k_y) = \sum_l \sum_m \sqrt{a(x_l, y_m)} g(x_l, y_m) \exp[-jk_x(x_l - v_{x_l}\tau) - jk_y(y_m - v_{y_m}\tau)] \quad (6)$$

where $g(\cdot)$ is the radar backscatter and $a(\cdot)$ is the measured antenna two-way beampattern. To convert this expression into the Doppler frequency domain, a change of variables can be used to map the spatial frequency to the Doppler frequency f , via $k_y = 4\pi f/c$ where c is the speed of light. As shown in Appendix A, the power spectral density relating to the Doppler frequency can be written as a convolution between the antenna beampattern, $A(f)$ and the underlying mean Doppler spectrum of the stationary and moving scatterers, $\Psi(f)$,

$$P_0(f) = A(f) \otimes_f \Psi(f) \quad (7)$$

where \otimes represents the convolution operator. The goal of this work is to characterise the underlying spectrum with realistic models to account for the different types of scattering. A simple Gaussian model is presented in Section 4, while a two component model is presented in Section 5. Furthermore, there are two measurement based additions that need to be included. These are the noise spectral density of the radar system, $P_n(f)$ and the $2Q$ alias components which are present when the sea-clutter is under sampled. These are described in the following two sections and are captured in the following modified model

$$P(f) = \sum_{q=-Q}^Q A(f + qf_{\text{PRF}}) \otimes_f \Psi(f + qf_{\text{PRF}}) + P_n(f) \quad (8)$$

where f_{PRF} is the PRF.

3.5 Noise spectral density of the radar system

This section shows how the noise spectral density can be determined from the mean instantaneous power (also known as the mean backscatter). If the autocorrelation of $X(t)$ is given by

$$R(\tau) = E[X(t)X^*(t - \tau)] \quad (9)$$

then the mean backscatter is equal to the autocorrelation at zero-lag, $R(0)$. The autocorrelation is also related to Doppler spectrum through the Wiener Khinchin theorem

$$R(\tau) = \int_{-\infty}^{\infty} P(f) \exp[j2\pi f\tau] df, \quad (10)$$

$$P(f) = \int_{-\infty}^{\infty} R(\tau) \exp[-j2\pi f\tau] d\tau. \quad (11)$$

Therefore, the mean backscatter can be related to the noise spectral density by

$$R(0) = \int_{-\infty}^{\infty} P(f) df. \quad (12)$$

For the full-pol data sets, the mean instantaneous thermal noise power of the radar system was estimated by processing part of the collection where the RF transmitter was turned off. By assuming the sea-clutter and thermal noise are independent throughout the processing chain, a simulated noise signal was then created in the backscatter coefficient domain. This signal has the same number of pulses and range bins as the clutter plus noise signal and undergoes the same pre-processing steps as the clutter plus noise signal in Figure 2. If this power is described by $R_n(0) = P_n(f)f_{\text{PRF}}$, then the noise spectral density which is constant over the whole frequency band is given by

$$P_n(f) = R_n(0)/f_{\text{PRF}}. \quad (13)$$

Using this approach, the noise estimates for the two data sets, F35 and F9 are shown in Figures 4-5.

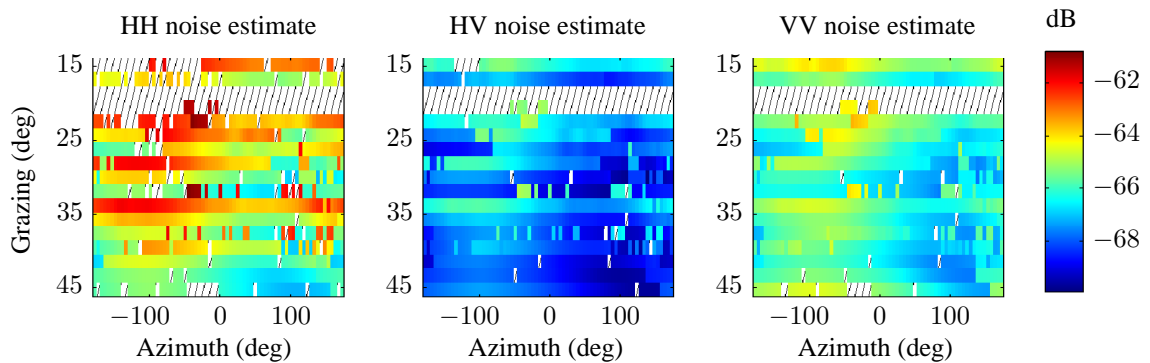


Figure 4: F35 noise estimate, left: HH, middle: HV, right: VV. Hashed areas indicate regions with poor or missing data.

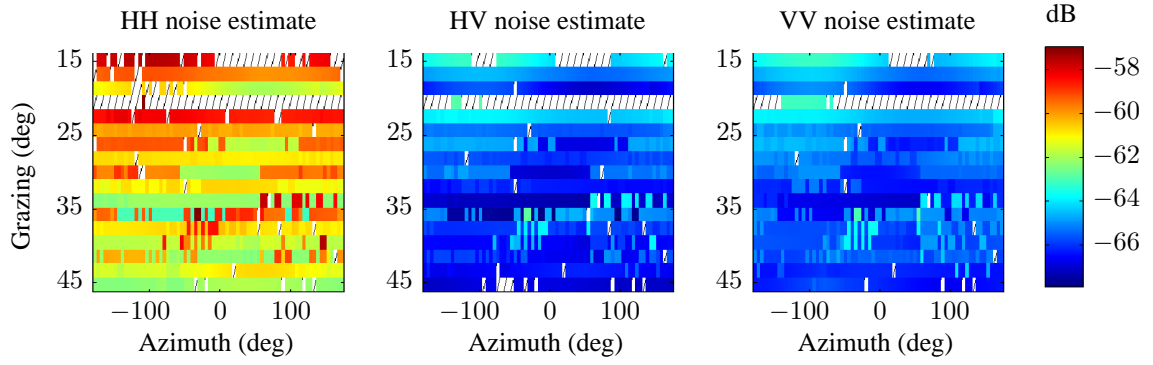


Figure 5: F9 noise estimate, left: HH, middle: HV, right: VV. Hashed areas indicate regions with poor or missing data.

3.6 Aliasing

Aliasing occurs when the combined bandwidth of the sea spectrum and the azimuth beampattern (due to the motion of the radar platform) exceed the PRF of the radar. The result is to raise the sides of the spectrum where the extra spectral content folds into the sampled region. To demonstrate how this effect is captured in Equation 8, consider the convolution of two Gaussian signals

$$b(f) = a_1 \exp \left[-\frac{(f - \mu_1)^2}{\sigma_1^2} \right], \quad (14)$$

$$w(f) = a_2 \exp \left[-\frac{(f - \mu_2)^2}{\sigma_2^2} \right]. \quad (15)$$

with magnitudes a_1, a_2 , centre frequencies μ_1, μ_2 and widths σ_1, σ_2 . An analytic form of the convolution can then be used to show how the different ‘aliased’ contributions combine together. The convolution of these two signals is derived in Appendix B,

$$\begin{aligned} P(f) &= \sum_{q=-Q}^Q b(f + qf_{\text{PRF}}) \otimes w(f + qf_{\text{PRF}}) \\ &= \sum_{q=-Q}^Q \frac{\sigma_1 \sigma_2}{\sqrt{\sigma_1^2 + \sigma_2^2}} \sqrt{\pi} \exp \left[-\frac{(f + qf_{\text{PRF}} - (\mu_1 + \mu_2))^2}{\sigma_1^2 + \sigma_2^2} \right]. \end{aligned} \quad (16)$$

Figure 6 shows an example of this convolution for $Q = 1$. The three components are shown in blue and red with the summation in black. This model can be implemented through the use of circular convolution, which essentially fixes $Q = 1$ in Equation 8. Analysis has shown that there is little benefit in accounting for the aliased components beyond this. Also, to ensure that the total energy remains the same before and after the convolution, the azimuth beampattern is normalised to have an area of 1.

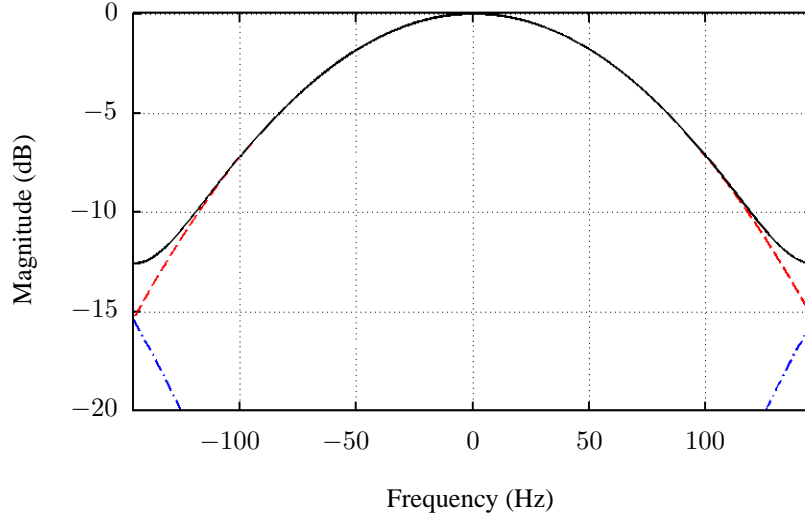


Figure 6: Aliasing example: (---) $q = \pm 1$, (- -) $q = 0$, (—) combined spectrum

3.7 Formation of the Doppler spectrum

There are a number of considerations which determine the appropriate data region for forming the Doppler spectrum. These include the geometry of the platform relative to the sea surface, the observation time and the number of range bins used to estimate the spectrum. To achieve a good estimate of the mean Doppler spectrum, a number of range bins must be averaged. Figure 7 shows an example of the same Doppler spectrum estimated over 10, 100 and 500 range bins. It is clear that increased averaging reduces fluctuations in the estimate. This does however require a wider span of grazing angles which limits the ability to determine the effect of small variations in grazing angle and can result in significant changes in the Doppler frequency associated with the azimuth beampattern.

To ensure that the spectrum is of reasonable quality for the subsequent analysis, the data is binned into 2° blocks of grazing angles. The observation time, T_{obs} is then carefully chosen to make sure that the Doppler frequency shift due to the angular motion of the aircraft has constant bin spacing and is linear over the resolution cells selected. To ensure the first constraint is met, the frequency resolution, $1/T_{\text{obs}}$ must not change by more than half a frequency bin. For the second constraint, consider the Taylor series expansion around $t = 0$,

$$\hat{f}(t|x_1, y_1) = \sum_{n=0}^{\infty} \frac{f^{(n)}(t|x_1, y_1)t^n}{n!} = \sum_{n=0}^{\infty} F_n(t|x_1, y_1). \quad (17)$$

To satisfy linearity over the observation time, the second term of the expansion must be significantly less than the first, $F_2(T_{\text{obs}}|x_1, y_1) \ll F_1(T_{\text{obs}}|x_1, y_1)$. If x_{\min} and x_{\max} are the minimum and maximum slant ranges from the centre of the swath and y_{\max} is the maximum one sided azimuth extent, then these two constraints can be used to determine the observation time,

$$\begin{aligned} \underset{T_{\text{obs}}}{\text{argmax}} \quad & |f(T_{\text{obs}}|x_{\max}, y_{\max}) - f(T_{\text{obs}}|x_{\min}, 0)| < \frac{1}{2T_{\text{obs}}} \\ \text{subject to} \quad & F_2(T_{\text{obs}}|x_{\max}, y_{\max}) \leq 0.1 F_1(T_{\text{obs}}|x_{\max}, y_{\max}). \end{aligned} \quad (18)$$

In the trial data, there are many runs which have common grazing angle regions and some which contain more than one orbit. To further maximise the observation time for the chosen geometry, each of these data blocks are analysed and the one with the best combination of observation time and the number of range (or grazing bins) is then selected and a periodogram is used to form an estimate of the mean Doppler spectrum. Figures 8-9 show the total number of range bins and the observation times for the two example data sets, F35 and F9. The first data set, F35 is from the 2004 trial, while the second data set F9, is from the 2006 trial. The mean number of range bins for these two days are 272 and 269, while the mean observation times are 1.56 s and 1.52 s respectively.

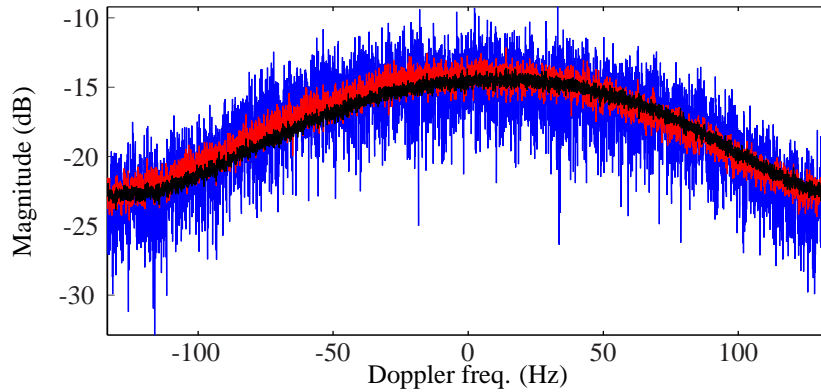


Figure 7: Doppler spectrum comparison, number averages: (—) 10, (—) 100, (—) 500

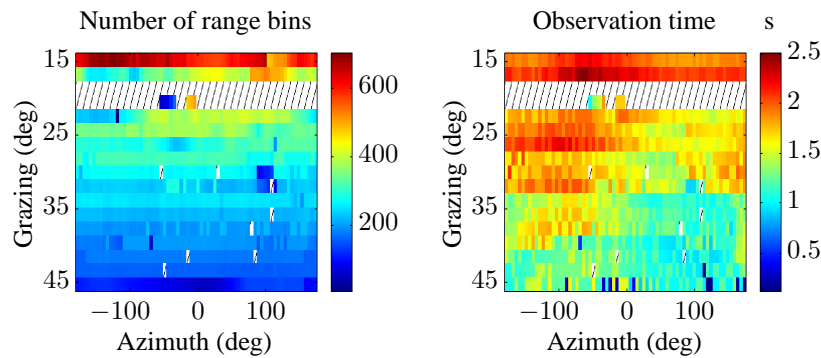


Figure 8: Total number of range bins and observation times used for estimates in F35. Hashed areas indicate regions with poor or missing data.

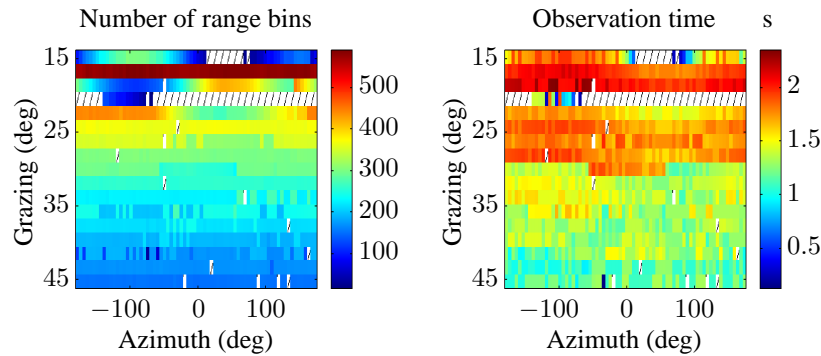


Figure 9: Total number of range bins and observation times used for estimates in F9. Hashed areas indicate regions with poor or missing data.

4 Sea-clutter analysis - single component model

This section considers a single Gaussian model for the underlying mean Doppler spectrum. While this is a simplistic model, it is useful for comparing with results in the literature and as a baseline against the new model in Section 5. The following Section 4.1 describes this single component model and how the model parameters can be estimated from the data. Model results are then presented in Section 4.2 for the upwind and downwind directions. Section 4.3 then looks at variations of model parameters over azimuth and grazing, while the last Section 4.4 looks at variations over different weather conditions including wind speed, wave height and wave period.

4.1 Single component fit

The Gaussian model is used by a number of authors to model the underlying Doppler spectrum [Hicks et al. 1960, Walker 2001a, Walker 2001b]. The form of the Gaussian lineshape is based on Walker's model and is the same for each polarisation channel

$$\begin{aligned}\Psi_{HH}(f) &= T_{HH} \exp \left[-\frac{(f - f_{HH})^2}{w_{HH}^2} \right], \\ \Psi_{HV}(f) &= T_{HV} \exp \left[-\frac{(f - f_{HV})^2}{w_{HV}^2} \right], \\ \Psi_{VV}(f) &= T_{VV} \exp \left[-\frac{(f - f_{VV})^2}{w_{VV}^2} \right]\end{aligned}\tag{19}$$

with magnitudes T_{HH}, T_{HV} and T_{VV} , centre frequencies, f_{HH}, f_{HV} and f_{VV} and widths w_{HH}, w_{HV} and w_{VV} . Using this form of the Gaussian, the 3 dB width is related to the width w by $w_{3dB} = 2\sqrt{\ln 2}w$.

The process of data fitting involves forming an estimate of the underlying spectrum, convolving it with the azimuth antenna beampattern and adding thermal noise according to Equation 8. The interior-point optimisation algorithm is then used to estimate the appropriate model parameters. This algorithm requires a user defined cost function to be minimised. If the data (in dB) is represented by $x(f)$, then the chosen cost function is the root mean square (RMS) of the difference between the data and the model fit, $g(f)$. The RMS error, E is formed over L points evenly spaced in the valid Doppler frequency range, $f_V \in [f_{\min}, \dots, f_{\max}]$

$$E = \sqrt{\frac{1}{L} \sum_{f_V} [x(f) - g(f)]^2}.\tag{20}$$

This algorithm allows extra constraints to be included at the expense of extra processing time. For the single component fit, the only constraints used are the lower and upper parameter bounds described in Table 4. These are the same for each polarisation with the exception of the lower magnitude bounds set at the appropriate noise floor, n_{HH}, n_{HV} and n_{VV} according to the relationship in Equation 13. Initial values for each parameter are set midway between the lower and upper bounds.

Once the model has been fitted to the data, a useful metric for determining the quality of the model fit is the normalised root mean square (NRMS) error. This metric varies between zero and

Table 4: Bounds used for the single component fit, magnitudes in dB, centre point and width in Hz

	T_{HH}	T_{HV}	T_{VV}	f_{HH}, f_{HV}, f_{VV}	w_{HH}, w_{HV}, w_{VV}
Lower bound	n_{HH}	n_{HV}	n_{VV}	-100	10
Upper bound	10	10	10	100	150

one, with a lower value indicating a better fit. It is related to the RMS error by

$$E_{\text{NRMS}} = \frac{E}{\max \{x(f)\} - \min \{x(f)\}}. \quad (21)$$

To ensure the quality of the results, the spread Doppler spectrum must have a dynamic range of at least 3 dB and the estimated fits must have a NRMS error of less than 0.1.

4.2 Doppler spectrum

Two example range/Doppler images from the F9 dataset are shown in Figures 10-11. These cover the upwind and downwind directions respectively and are centred at 30° grazing. To form these images, two blocks of data were selected for the two wind directions spanning 1.8 s and 1.4 s respectively over a 2° grazing angle region. Wave structure can clearly be seen over a range of different Doppler frequencies. There are also clear periodic variations along the spatial dimension which will be averaged out when the mean Doppler spectrum is formed. A separate study along the lines of Watts [2012] is therefore required to assess this aspect of the Doppler spectrum evolution.

The corresponding mean Doppler spectra are shown in Figures 12-13 with the spread spectra on the left and underlying spectra on the right. Recall the spread spectrum includes the effect of the azimuth beam pattern, while the underlying spectrum has been formed using the estimated parameters with the models in Equation 19.

The model fit for the spread spectrum is very good with a NRMS error of less than 0.05 for each channel. The underlying spectrum was constructed with the parameter estimates given in Table 5. From these results, the VV channel is larger by 6-9 dB than the HH channel and 14-16 dB for HV. Also, between the two look directions, the magnitudes are between 2-4 dB. For the centre point, recall that the VV channel has been centred at the origin, with the other channels shifted relatively. The HH value shifts differently for each wind direction which is expected as the waves are moving in opposite directions with respect to the radar. With regard to the spectral widths, the HH results are slightly wider than the other two channels and between wind directions, the difference is between 10-20 Hz.

Table 5: Full-pol model single component model parameters, magnitudes in dB, centre points and widths in Hz

	T_{HH}	T_{HV}	T_{VV}	f_{HH}	f_{HV}	f_{VV}	w_{HH}	w_{HV}	w_{VV}
Upwind	-44.40	-54.02	-38.96	22.05	4.07	1.09	59.71	47.60	47.54
Downwind	-45.57	-51.28	-36.77	-38.55	-21.70	-2.59	46.62	25.00	28.68

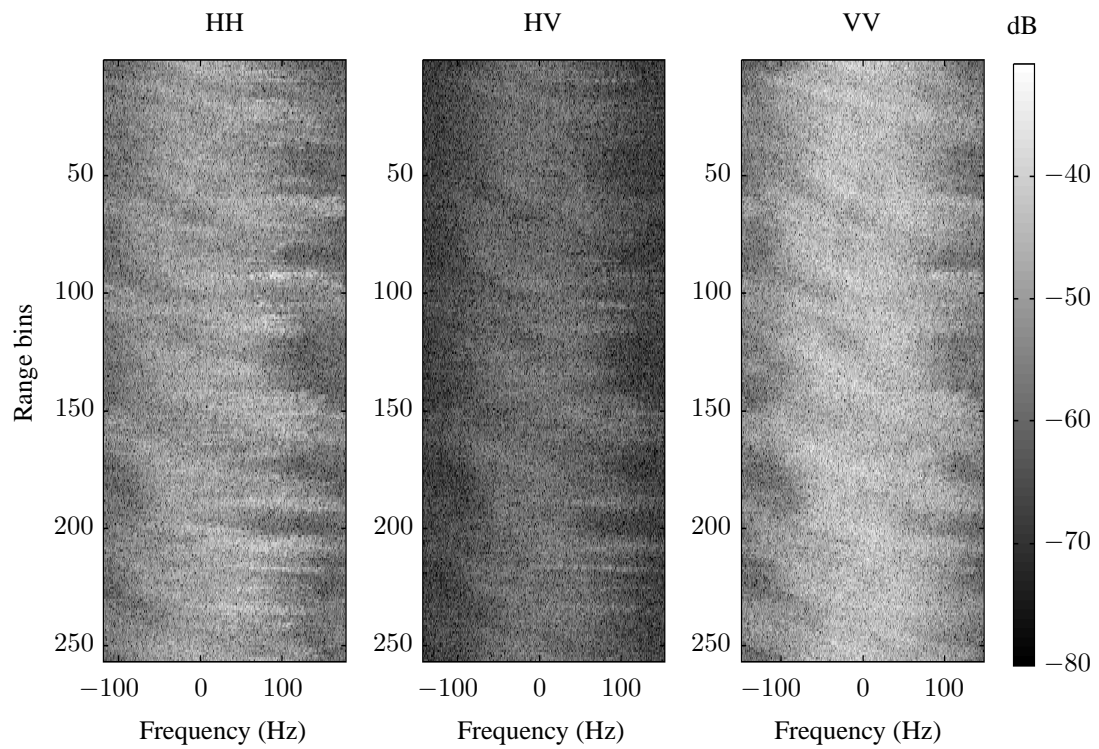


Figure 10: Full-pol upwind range/Doppler sea-clutter image

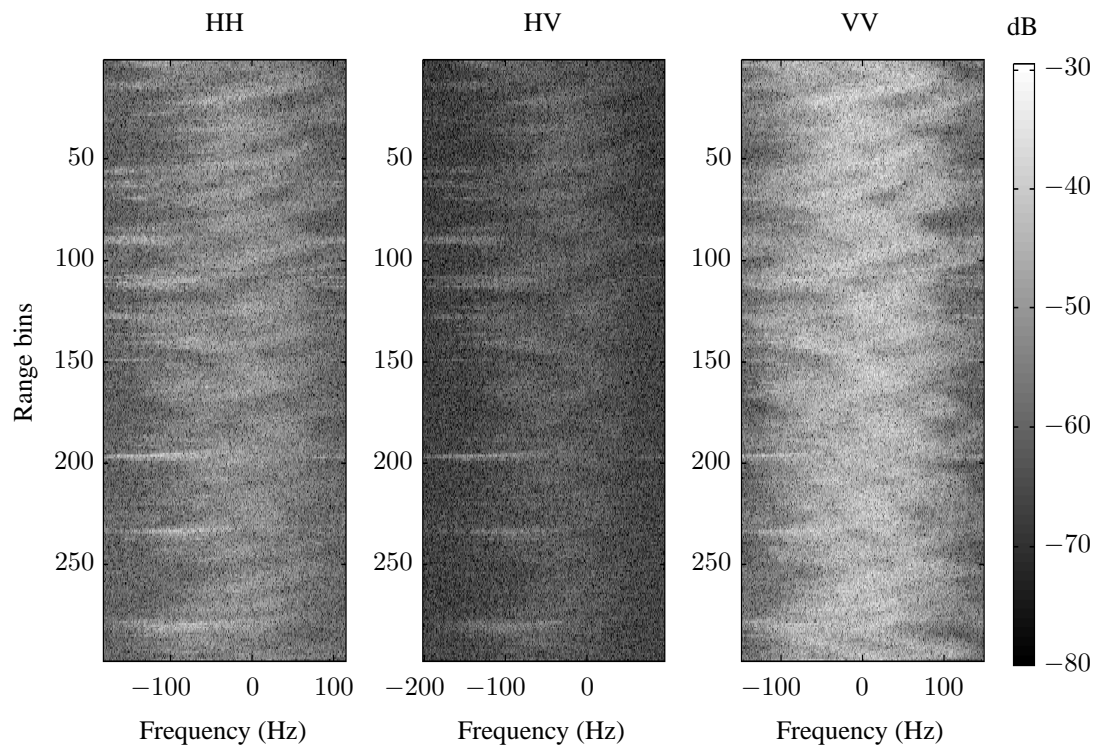


Figure 11: Full-pol downwind range/Doppler sea-clutter image

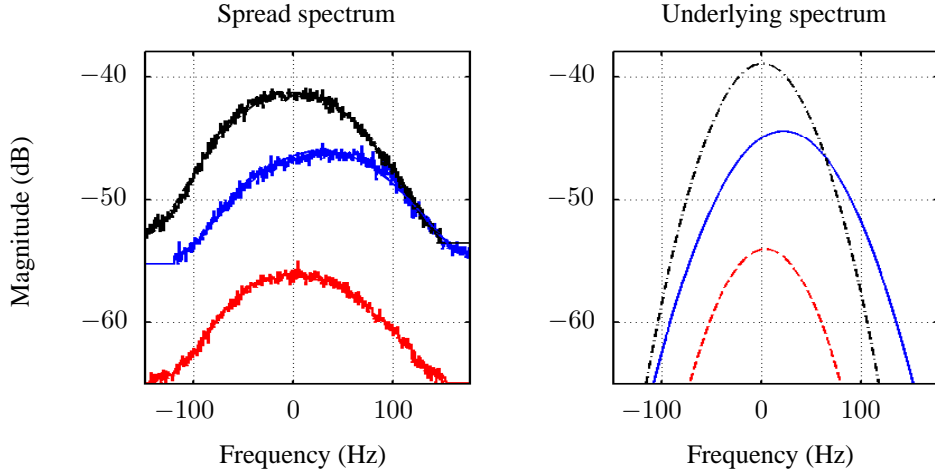


Figure 12: Full-pol upwind mean Doppler spectrum with single component model, spread spectrum on left, estimated underlying spectrum on right, (—) HH, (--) HV, (-.-) VV

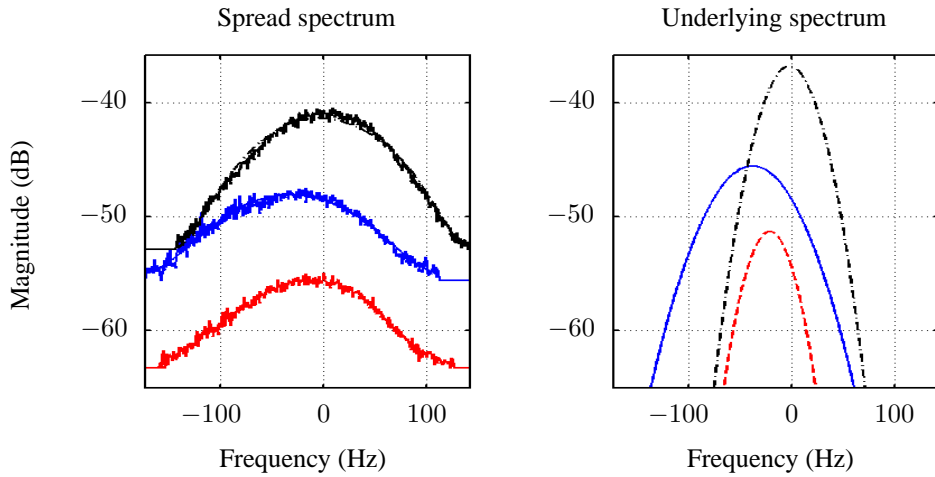


Figure 13: Full-pol downwind mean Doppler spectrum with single component model, spread spectrum on left, estimated underlying spectrum on right, (—) HH, (--) HV, (-.-) VV

4.3 Single component variation over geometry - full-pol

To study the relationship between model parameters and the collection geometry, this section looks at parameter variations over azimuth and grazing angles. The first set of results relate to the F35 dataset. Figure 14 shows the magnitude components for each polarisation, T_{HH} , T_{HV} and T_{VV} . The trend for these components is increasing magnitude with increasing grazing and a sinusoidal variation over azimuth with the largest value in the upwind direction. The strongest magnitude is found in the VV channel at -32 dB, while the HH and HV channels are approximately lower by 6 dB and 15 dB respectively.

Figure 15 shows the centre points, f_{HH} , f_{HV} and f_{VV} for each polarisation. As the spectrum is centred around the VV channel, the estimated centre point for this channel lies very close to 0 Hz. When the grazing angle is 15° , the HH channel has a peak of 75 Hz which decreases to 0 Hz.

20 Hz as the grazing angle increases to 45° . Along azimuth, the largest centre point is in the upwind direction while the downwind direction is strongly negative. The HV centre point has a smaller variation between -50 to 0 Hz and rarely lies between the HH and VV values.

The next Figure 16 then shows the widths, w_{HH} , w_{HV} and w_{VV} for each polarisation. Based on the studies by [Valenzuela & Laing 1970, Lee et al. 1995a], the expected results are that the bandwidth is greatest upwind and smallest in the downwind, the VV polarisation is almost independent of grazing angle and the HH width decreases to the VV level as the grazing angle increases. The first observation reflecting the differences in upwind and downwind is not apparent from these results which appear quite random with few discernable trends. The second observation relating the HH and VV channels is apparent, however with the HH component being much larger than VV at lower grazing angles. Then, as the grazing angle increases, this difference becomes smaller until it resembles the VV width at 40° and above.

One final observation is based on the the relationship in Equation 12. Since the analytic expression for the total power (area under a Gaussian) is given by

$$R(0) = \sqrt{\pi}Tw \quad (22)$$

are due to the small variation in the spectral width, the trends observed with the magnitudes match those of the mean backscatter shown in Figure 17. Further information on the mean backscatter can be found in the paper by Crisp et al. [2008].

The second set of results for F9 are shown in Figures 18-21. The mean and magnitude components are again very similar, while the results for the centre point in Figure 19 reflect the same trends as F35 with slightly smaller values.

For the spectral width in Figure 20, the HH channel now has a discernable trend in the upwind direction at lower grazing angles. A peak width of 110 Hz is seen at 15° grazing which reduces to 10 Hz at 45° . This trend is not observed in the other two polarisation channels which have values similar to F35. Further analysis of the other data sets revealed only a few days with this trend.

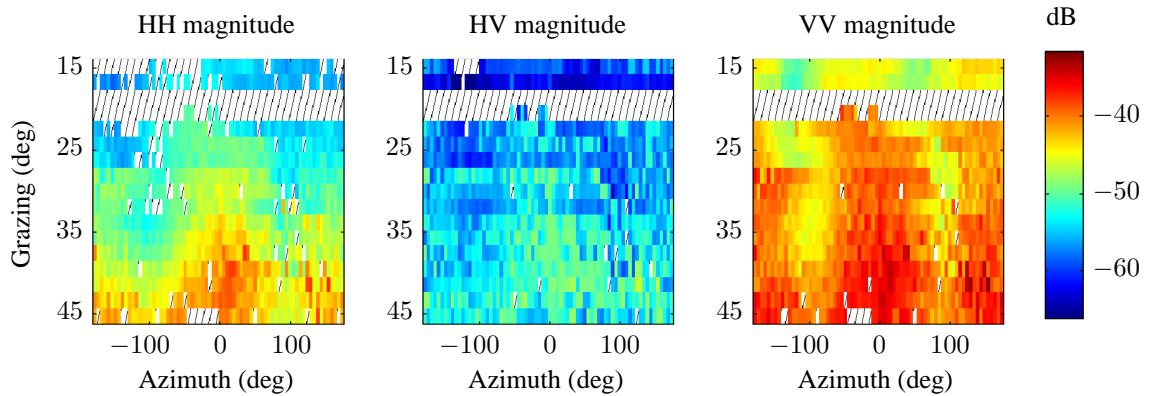


Figure 14: Single component fit for F35, magnitude, left: HH, middle: HV, right: VV. Hashed areas indicate regions with poor or missing data.

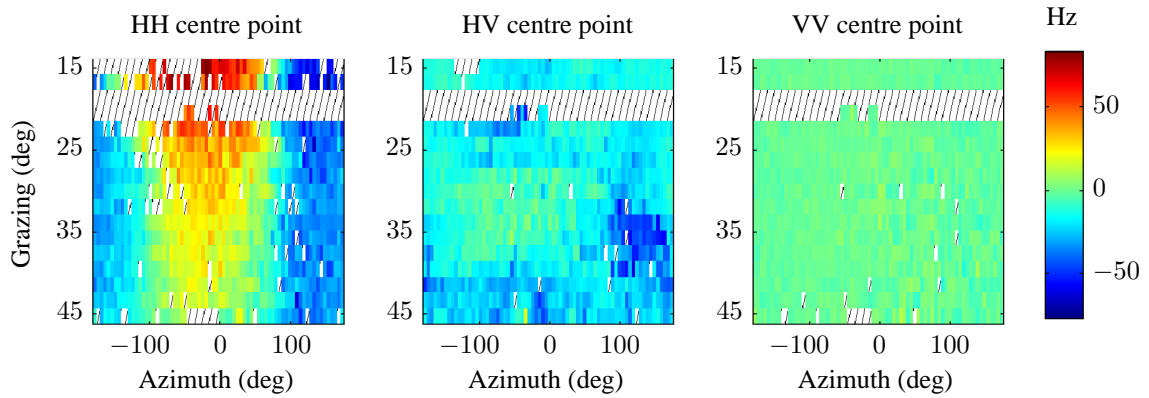


Figure 15: Single component fit for F35, centre point, left: HH, middle: HV, right: VV. Note that the VV channel is shifted to have a Doppler centroid of 0 Hz with the HH and HV channels shifted relatively. Hashed areas indicate regions with poor or missing data.

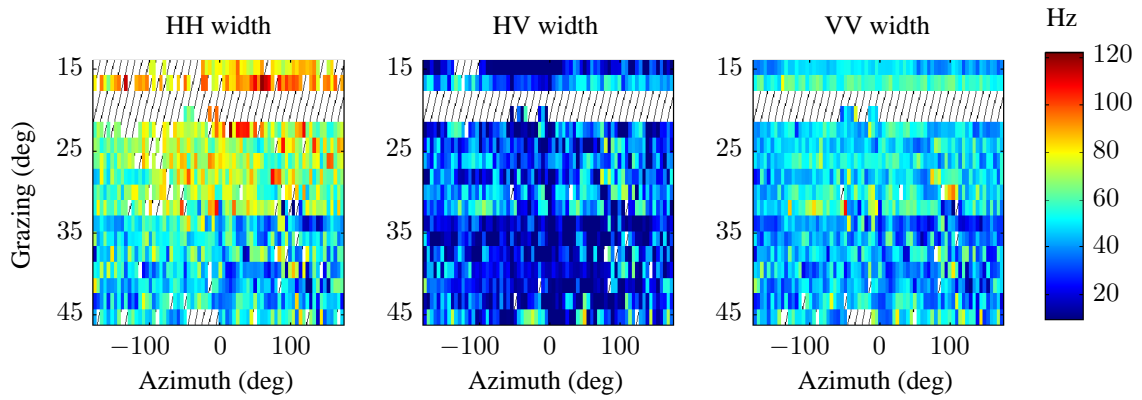


Figure 16: Single component fit for F35, width, left: HH, middle: HV, right: VV. Hashed areas indicate regions with poor or missing data.

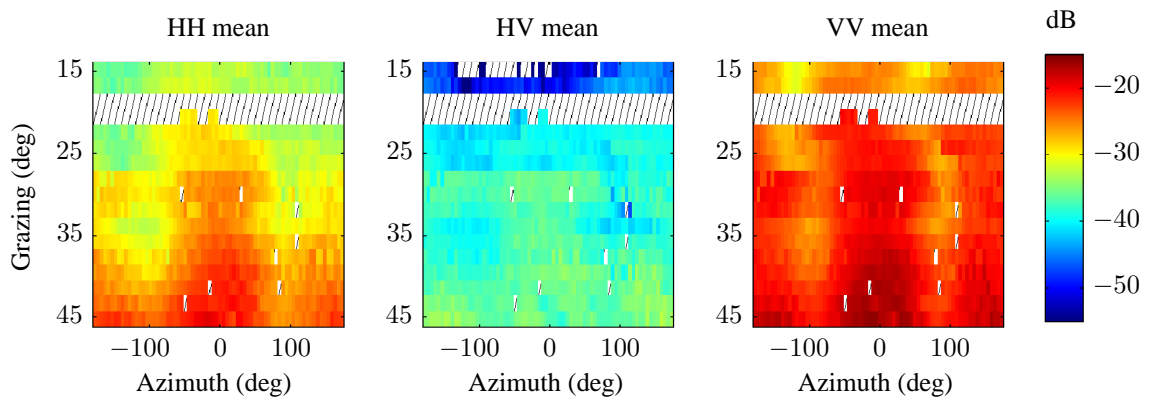


Figure 17: F35 mean backscatter, left: HH, middle: HV, right: VV. Hashed areas indicate regions with poor or missing data.

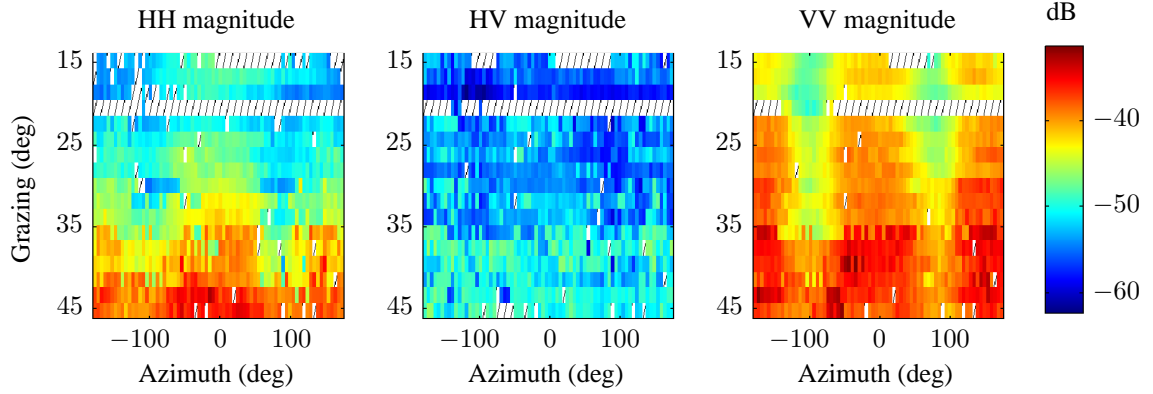


Figure 18: Single component fit for F9, magnitude, left: HH, middle: HV, right: VV. Hashed areas indicate regions with poor or missing data.

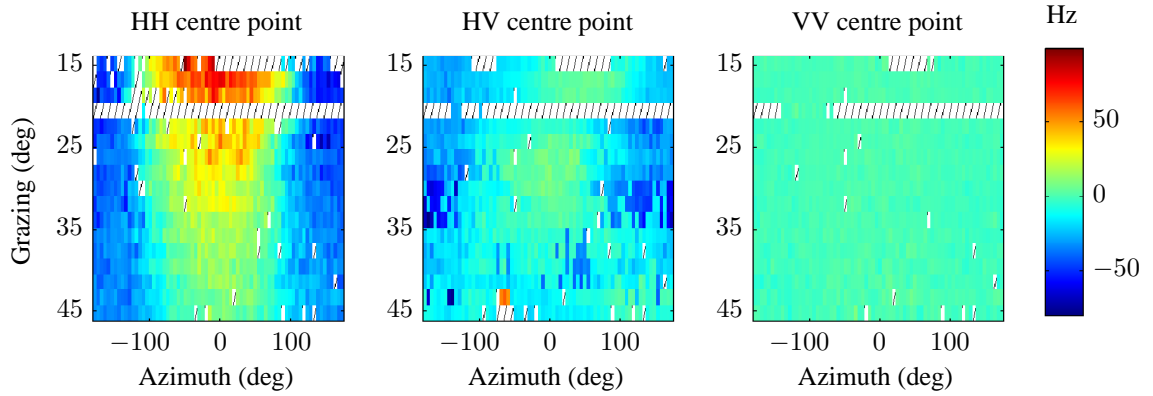


Figure 19: Single component fit for F9, centre point, left: HH, middle: HV, right: VV. Note that the VV channel is shifted to have a Doppler centroid of 0 Hz with the HH and HV channels shifted relatively. Hashed areas indicate regions with poor or missing data.

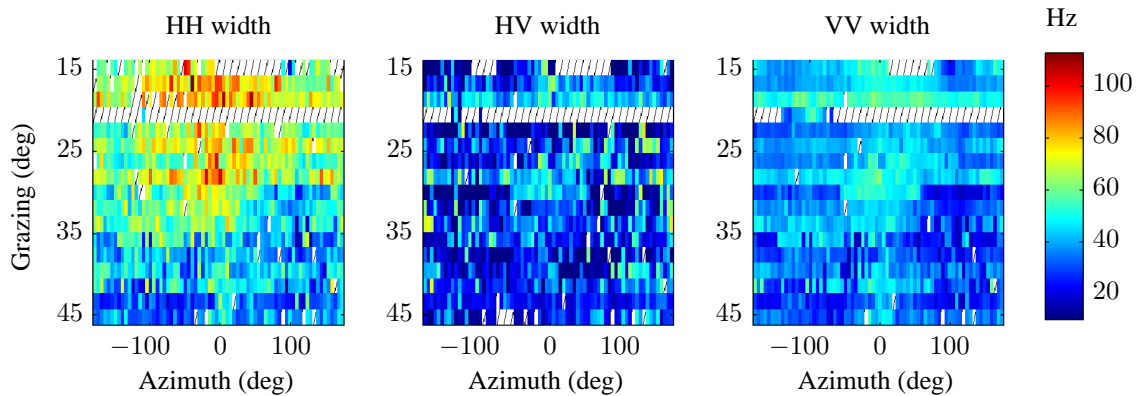


Figure 20: Single component fit for F9, width, left: HH, middle: HV, right: VV. Hashed areas indicate regions with poor or missing data.

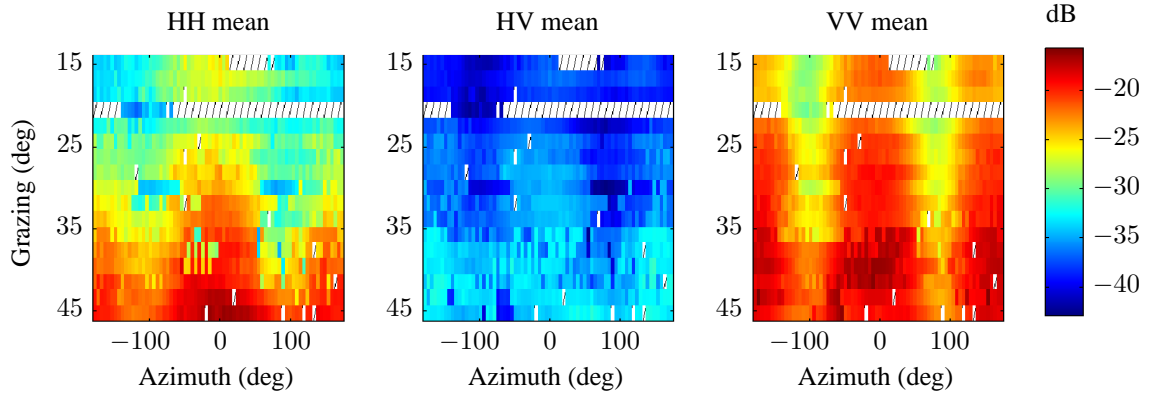


Figure 21: F9 mean backscatter, left: HH, middle: HV, right: VV. Hashed areas indicate regions with poor or missing data.

4.4 Variation in sea conditions

As the sea state increases, the wind speed, wave height and period all increase. These will in turn increase the magnitude and width of the Doppler spectrum, [Hicks et al. 1960, Bass et al. 1968, Valenzuela & Laing 1970, Duncan, Keller & Wright 1974]. This section looks at how the model parameters vary with different sea conditions in order to verify these results for higher grazing angles.

The first result in Figure 22 looks at the model magnitudes for all data sets as a function of wind speed in the upwind direction with 30° grazing. As expected, each of the components increase with wind speed and a power-law fit has been used to represent the trends with RMS errors of 1.93, 1.59 and 1.49 dB for the three channels respectively.

For the second result, Hicks et al. [1960] has shown experimentally that the Doppler width at high grazing angles is proportional to the wave height divided by the wave period. A further study by Bass et al. [1968] confirmed the relationship between wave height and period at lower grazing angles. Figure 23 shows the widths as a function of wave height / wave period, also in the upwind direction with 30° grazing. There is a clear increasing linear trend with RMS errors of 10.92, 13.67 and 8.21 Hz for the three channels respectively.

The sea conditions of the two trials differed due to a swell which was present in the Port Lincoln trial but not in Darwin. This resulted in higher waves for the former data set and significantly wider spectral widths. Analysis of these values showed a trend only in the HH channel for the F9 dataset. Consequently, the final results look at variation of the mean width averaged over all grazing and azimuth angles as a function of the measured wind speed and wave height.

The first component of the model is a vector of wind speeds ordered from slowest to fastest, \mathbf{U} , the second are the corresponding wave heights, \mathbf{W} and the third are the corresponding mean spectral widths, \mathbf{S} . Since the analysis contains 12 days of data, each of these vectors are size 12×1 . The equation relating the three components is given by

$$\begin{aligned}
 \mathbf{S} &= a_0 + a_1 \mathbf{U} + a_2 \mathbf{W} \\
 &= [\mathbf{1}_{12 \times 1} \quad \mathbf{U} \quad \mathbf{W}] [a_0 \quad a_1 \quad a_2]^T \\
 &= \mathbf{Y} \mathbf{A}
 \end{aligned} \tag{23}$$

where \mathbf{Y} is size 12×3 . This equation can be solved using a least square solution

$$\mathbf{A} = [\mathbf{Y}^T \mathbf{Y}]^{-1} \mathbf{Y}^T \mathbf{S}. \quad (24)$$

To recreate the model for a given wind speed, U and wave height, W , a scalar version of Equation 23 can be used

$$S = a_0 + a_1 U + a_2 W \quad (25)$$

with the coefficients given in Table 6. Figures 24 - 26 show this model which has been fitted to the data with RMS errors of 5.94, 3.04 and 3.08 Hz for the three channels respectively. This result demonstrates that the width can be well represented as a function of both wind speed and wave height and hence the ocean is not fully developed. Also, compared to the HH channel, there is a smaller variation in the width for the HV channel and to a lesser extent, the VV channel.

Table 6: Sea variation width model coefficients

	HH	HV	VV
a_0	-4.00	-1.72	0.67
a_1	4.57	2.37	2.96
a_2	6.44	3.81	5.93

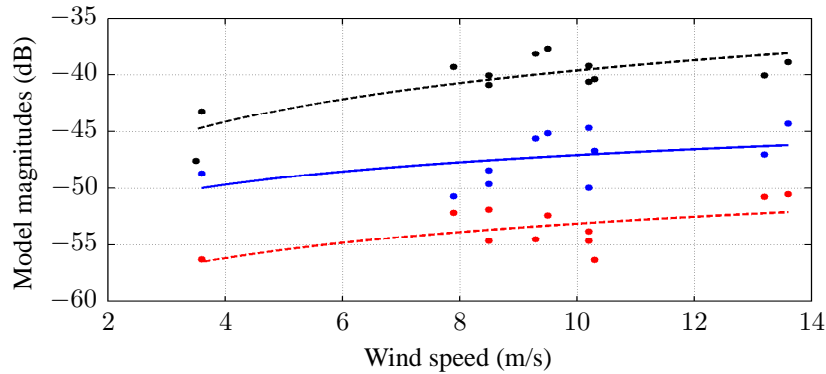


Figure 22: Model magnitudes as a function of wind speed, upwind, 30° grazing, (—) HH, (--) HV, (.-) VV

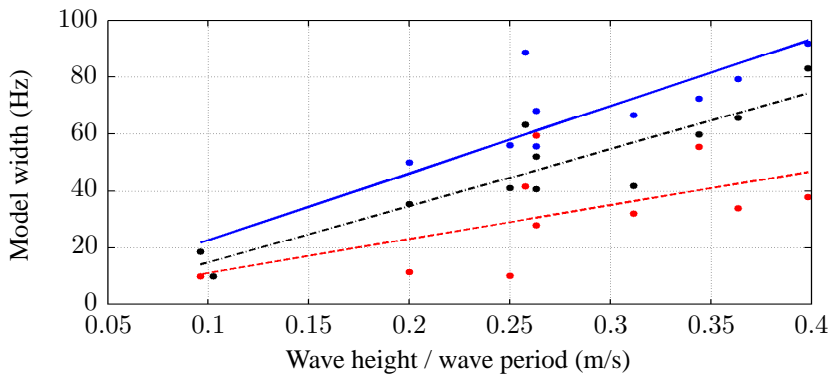


Figure 23: Model width as a function of wave height / wave period, upwind, 30° grazing, (—) HH, (--) HV, (.-) VV

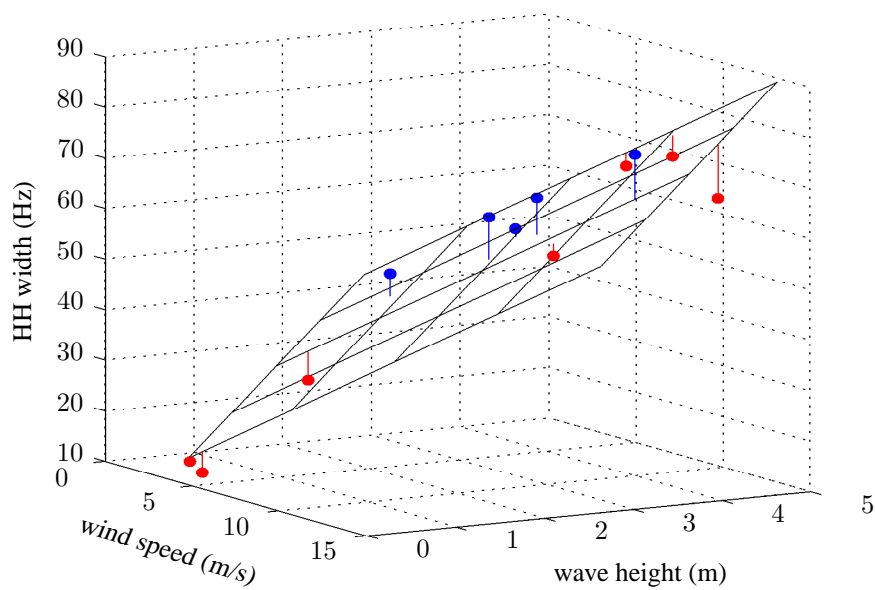


Figure 24: HH width as a function of wind speed and wave height

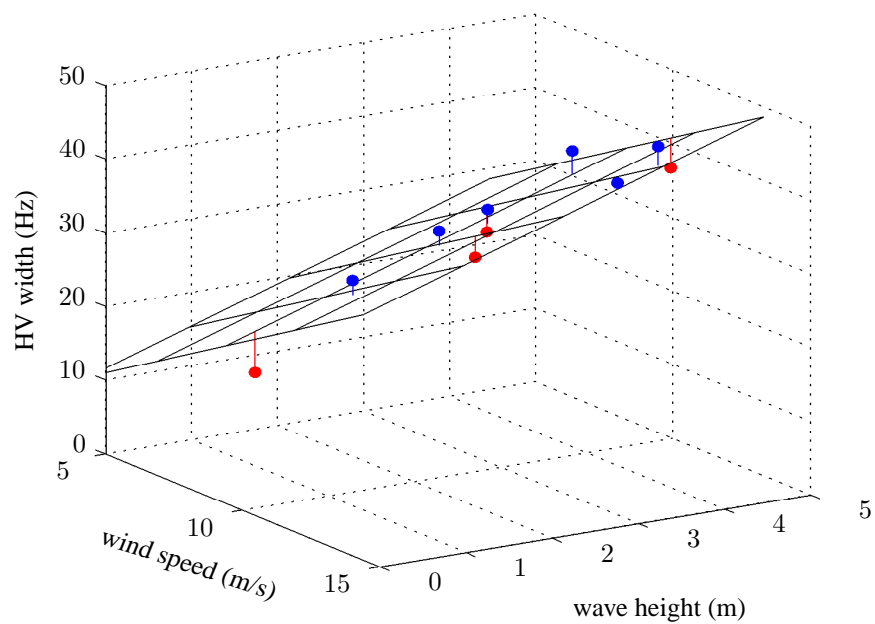
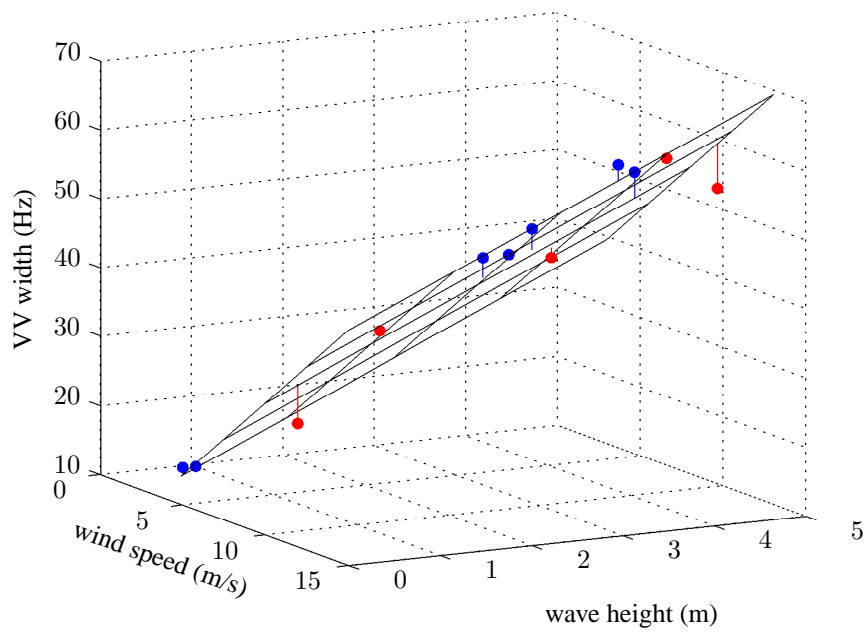


Figure 25: HV width as a function of wind speed and wave height



5 Two component model

This section describes a new two component underlying Doppler spectrum model which captures both the slow Bragg and the fast non-Bragg scattering from the sea-clutter. This model is then used in the following section for characterising the dual and full-pol Ingara data sets.

The two component Doppler model is described in Section 5.1 and is based on observations from the literature study in Section 2 and the analysis by Rosenberg [2012b]. The accuracy of the estimated model parameters are then demonstrated with simulated data for both dual and fully polarised collection modes. The simulation is described in Section 5.2 with an analysis of the accuracy given in Section 5.3.

5.1 Two component model

The new two component model uses the Gaussian building blocks that both [Walker 2000, Walker 2001a, Walker 2001b] and Lamont-Smith [2004] used. A number of observations from the literature influenced the new model:

- Breaking waves are faster than Bragg waves and thus possess high Doppler velocities, [Melief et al. 2006].
- Sea-spikes are visible at all grazing angles, [Lee et al. 1995a, Rosenberg 2012b].
- At higher grazing angles, the Doppler spectrum for both HH and VV are similar, ie. no Brewster angle damping is present, [Lee et al. 1995a].
- Both discrete and persistent non-Bragg scatterers are present in both HH and VV channels, [Rosenberg 2012b].

The model is based on these considerations and also the fact that the majority of the Ingara data has been collected at a low PRF making estimation of too many parameters difficult. This model differs to Walker's model in that the persistent whitecap and discrete sea-spike components have been combined into a single component which is present in both HH and VV. The two component model² is given by

$$\begin{aligned}\Psi_{HH}(f) &= \Psi_{S_{HH}}(f) + \Psi_{F_{HH}}(f), \\ \Psi_{VV}(f) &= \Psi_{S_{VV}}(f) + \Psi_{F_{VV}}(f)\end{aligned}\tag{26}$$

where the first component for each polarisation represents the slow Bragg component with the same centre frequency f_S and width, w_S and each polarisation has a different magnitude, S_{HH} and S_{VV} . The centre frequency is related to the Bragg speed by $f_S = 2v_S/\lambda$.

$$\begin{aligned}\Psi_{S_{HH}}(f) &= S_{HH} \exp \left[-\frac{(f - f_S)^2}{w_S^2} \right], \\ \Psi_{S_{VV}}(f) &= S_{VV} \exp \left[-\frac{(f - f_S)^2}{w_S^2} \right].\end{aligned}\tag{27}$$

²If the cross-pol channel was available, it could be included with a unique magnitude for the slow and fast components and the same centre frequencies and widths as the other two channels.

The second component represents the fast non-Bragg component associated with both the discrete and persistent sea-spikes. It is assumed that the sea-spike return is present in both polarisations with the same centre point, f_F and width w_F , but different magnitudes F_{HH} and F_{VV} .

$$\begin{aligned}\Psi_{F_{HH}}(f) &= F_{HH} \exp \left[-\frac{(f - f_F)^2}{w_F^2} \right], \\ \Psi_{F_{VV}}(f) &= F_{VV} \exp \left[-\frac{(f - f_F)^2}{w_F^2} \right].\end{aligned}\tag{28}$$

Similarly to the single Gaussian model in Section 4.1, the process of data fitting involves forming the underlying spectrum and convolving it with the azimuth beampattern according to Equation 8. The interior-point optimisation algorithm is then used to estimate the appropriate model parameters. To extend the cost function from Equation 20 to cover multiple polarisations, the difference between the model and data for each polarisation is combined into a vector. For example, If the HH and VV data (in dB) is represented by x_{HH} and x_{VV} , then the RMS error between the data and the model fit, g_{HH} and g_{VV} is given by

$$\tilde{E} = \sqrt{\frac{1}{L} \sum_{f_V} [x_{HH}(f) - g_{HH}(f), x_{VV}(f) - g_{VV}(f)]^2}.\tag{29}$$

For each parameter, realistic lower and upper bounds have been chosen through a combination of experimentation and a study of similar parameters from the literature. The bounds are described in Table 7 with the lower magnitude bounds set at the appropriate noise floor, n_{HH} and n_{VV} according to the relationship in Equation 13. Initial values for each parameter are set midway between the lower and upper bounds.

Table 7: Bounds and initial values for the two component model fit, magnitudes in dB, centre points and widths in Hz

	S_{HH}	S_{VV}	f_S	w_S	F_{HH}	F_{VV}	f_F	w_F
Lower bound	n_{HH}	n_{VV}	-50	20	n_{HH}	n_{VV}	-100	20
Upper bound	10	10	50	80	10	10	100	120
Initial values	-10	0	0	50	-10	-10	0	60

Finding the ‘best’ combination of parameters for the two component model is difficult as there are often a number of good solutions to the optimisation problem. The goal is to find a solution with a low RMS error and a parameter set which does not significantly deviate from other data points with similar geometry. To better guide the solution, a number of extra constraints are used

$$\begin{aligned}S_{VV} &> S_{HH}, \\ S_{VV} - S_{HH} &< 20\text{dB}, \\ F_{HH} - F_{VV} &< 15\text{dB}, \\ |f_F| &> |f_S|, \\ w_F &> w_S.\end{aligned}\tag{30}$$

The first constraint relates to the slow magnitude to ensure that the VV component is always greater than HH. The second and third ensure that for each component, the separation between

HH and VV is realistic. The final two constraints then ensure that the fast component is always faster than the slow component and that the fast spectral width is always greater than the slow width. Note that due to the arbitrary zero frequency, there is no constraint to ensure the sign of the fast component is the same as the slow component. To ensure the quality of the results, each of the estimated fits must have a dynamic range of at least 3 dB and an NRMS of less than 0.1.

5.2 Simulation

To verify the accuracy and robustness of the fitting process, a simulation of the Doppler spectrum has been performed. Figure 27 shows the procedure where a set of model parameters are used to generate an underlying Doppler spectrum which is convolved with the Ingara azimuth beam-pattern. The parameter choices were chosen so that they did not violate either the bounds or the extra constraints described in Equation 30. To increase the realism of the simulation, thermal and speckle noise are included as two exponential random vectors. The thermal noise is added to the Doppler spectrum, while the speckle noise is multiplied. To account for the averaging over range bins, N_{avg} realisations of each vector are generated and then averaged. The final result is a Doppler spectrum with similar characteristics to the received Ingara data. Table 8 shows the relevant parameters used for the simulation.

Table 8: *Relevant simulation parameters*

Parameter	Value
Centre frequency	10.1 GHz
Dual-pol PRF	600 Hz
Full-pol PRF	300 Hz
Platform velocity	90 m/s
Speckle mean	1
Noise power	-30 dB
Number of pulses, M	2000
Number of range bins, N_{avg}	300

The verification procedure takes the noisy Doppler spectrum and estimates the original model parameters. Then using these estimated values, the underlying Doppler spectrum can be reconstructed. To determine the accuracy of the model fit, both the estimated ‘spread’ Doppler spectra and the reconstructed underlying Doppler spectra can then be compared to their equivalent specified versions. Examples for both the dual and full-pol cases are shown in Figures 28 and 29 using the model parameters in Table 9. For each figure, the top plot shows the noisy spread spectra with the corresponding fit and the bottom plot shows the original and reconstructed underlying spectrum. Table 9 also shows the estimated parameters for each example which are very close to the specified values.

The mean NRMS error over the two polarisation channels for the dual-pol spread Doppler spectra is 0.0091 and for the underlying spectra is 0.0014. For the full-pol example, the mean NRMS error is slightly higher with 0.023 and for the underlying spectrum is 0.0014. For both cases, the spread values are slightly higher due to the thermal and speckle noise present in the simulated spectrum.

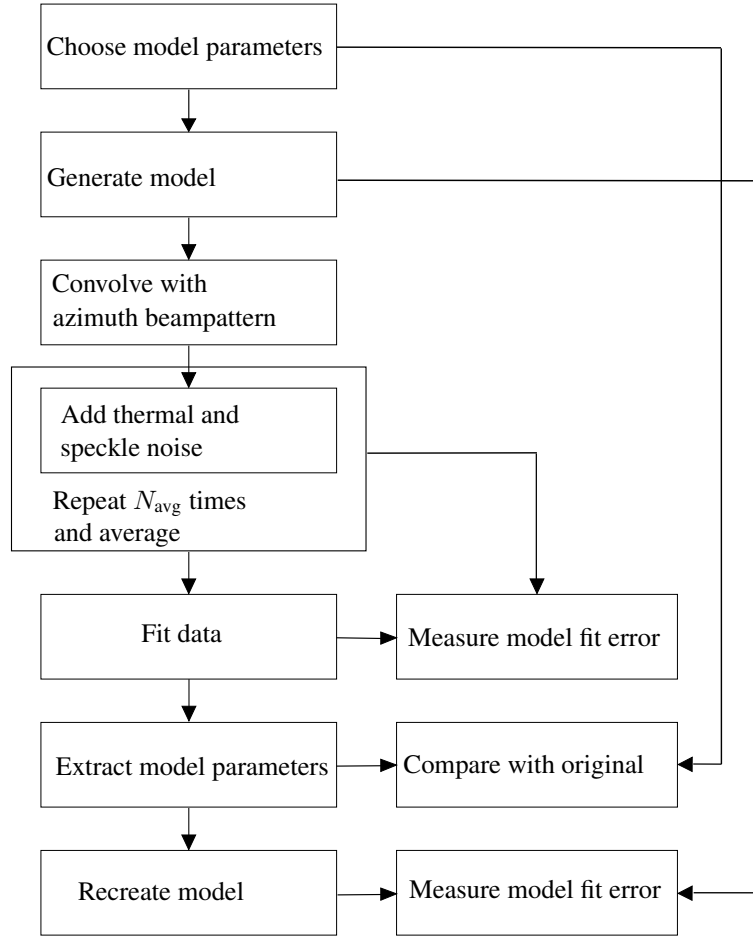


Figure 27: Verification block diagram

Table 9: Model parameters and estimation errors for simulation example, magnitudes in dB, centre points and widths in Hz

	S_{HH}	S_{VV}	f_S	w_S	F_{HH}	F_{VV}	f_F	w_F
Actual	-10	0	0	40	-10	-20	80	80
Estimated dual-pol	-10.07	0.014	-0.076	39.90	-10.00	-19.96	79.65	80.17
Estimated full-pol	-9.99	-0.019	0.025	40.00	-10.04	-20.03	80.39	80.49

5.3 Fitting accuracy

To verify the fitting accuracy of the two component model, a series of monte-carlo simulations are performed for both the dual and full-pol collection modes. The simulation procedure is repeated with 1000 different random parameter sets to determine the robustness of the fitting method and the accuracy of final parameter estimation. The range of parameter values and initial conditions used in the simulation are summarised in Table 10.

Two experiments were conducted for the dual and full-pol cases. Figures 30 and 31 show the respective scatter plots for each parameter with the correctly estimated parameters lying closely on the diagonal line. From experimental analysis, it was found that often the two centre points, f_S and

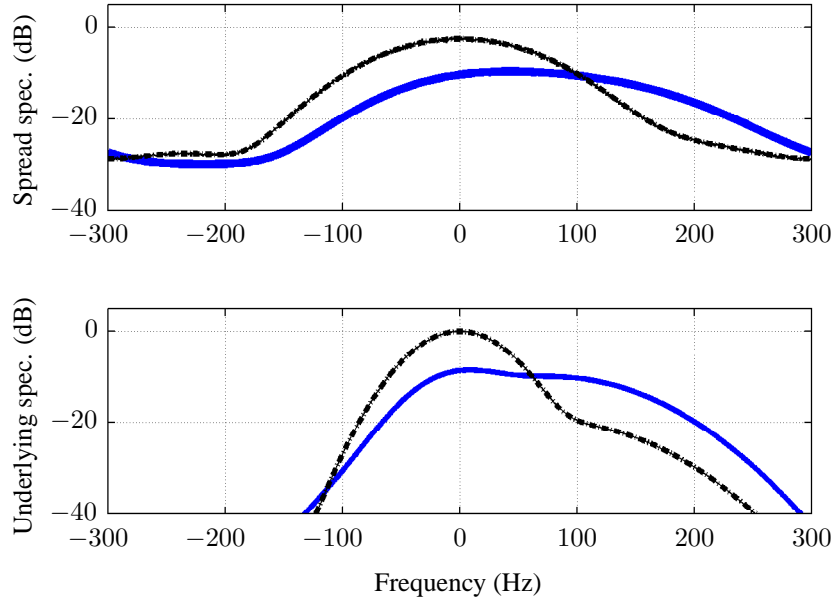


Figure 28: Example Doppler spectrum fits for dual-pol simulation (dB), (—) HH, (---) VV

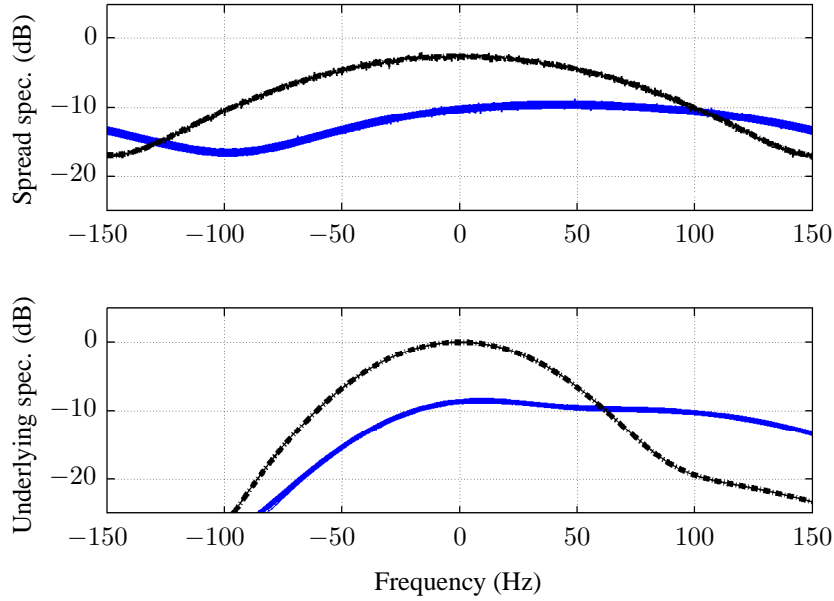


Figure 29: Example Doppler spectrum fits for full-pol simulation (dB), (—) HH, (---) VV

f_F can be confused in the fitting algorithm when they are close together. As a consequence, the monte-carlo analysis only considers the case where $|f_S - f_F| > 10$. Combined with the constraint that $|f_S| < |f_F|$, there is a small region where there are no valid points, ie. $-10 < f_F < 10$.

To measure the goodness of fit, a number of statistical measures were considered such as the chi-squared and one-sided t-test. It was found that a simpler method of comparison was to calculate the NRMS error between the ideal and the estimated version of both the spread and

Table 10: Range of model parameters and initial conditions used in verification, magnitudes in dB, centre points and widths in Hz

	S_{HH}	S_{VV}	f_S	w_S	F_{HH}	F_{VV}	f_F	w_F
Starting range	-20	-15	-50	20	-20	-20	-100	20
Ending range	0	5	50	80	0	0	100	120
Initial values	-10	0	0	40	-10	-10	0	60

underlying spectrums. For the dual-pol case, the percentage of mean NRMS errors within 0.05 is 97.25% for the spread Doppler spectrum and 94.98% for the underlying spectrum. For the full-pol case this reduces to 95.30% and 94.31% respectively. These results show that the model fitting is working to a very high level of accuracy, with the fit to the spread spectrum being slightly better than the underlying spectral fit and the dual-pol case being slightly better than the full-pol.

To compare the accuracy of the parameter estimation, a relative measure of error is calculated for each parameter by taking the magnitude of the difference between the estimated value and the desired one and then normalising by the expected range of parameter values. If p is an arbitrary parameter, then the parameter estimation error, p_{err} as a percentage is given by,

$$p_{\text{err}} = \frac{100|\hat{p} - p|}{p_{\text{max}} - p_{\text{min}}} \quad (31)$$

where p_{min} and p_{max} are the minimum and maximum parameter values. The mean parameter deviation has been calculated and is shown in Tables 11 and 12 for the dual and full-pol collection modes. In addition to this, the correlation coefficient has been calculated as an indication of the linear dependence between the desired and estimated parameters.

The dual-pol scatter plot shows a small mean deviation in the parameter estimates, with most being less than 1% and having a high correlation. This demonstrates that the dual-pol estimation procedure is working to a high degree of accuracy. The full-pol results show more variation than the dual-pol, due to the complication of the aliased spectrum. This results in the potential of different combinations of model parameters which can result in a good fit. The mean variation is still reasonable however with the majority of mean deviations less than 5%. The most difficult parameters to estimate are slow HH and fast VV magnitudes and the fast spectral width. The majority of the bad magnitude fits are only minor with the result being a lower correlation value. The fast width however still maintains a reasonable correlation implying that there are less bad estimates, but they are further from the true values.

Table 11: Dual-pol parameter deviation error and correlation values

	S_{HH}	S_{VV}	f_S	w_S	F_{HH}	F_{VV}	f_F	w_F
Deviation (%)	0.85	0.24	0.37	0.61	1.22	1.71	0.73	0.12
Correlation	0.99	1.00	1.00	1.00	0.99	0.97	0.99	1.0

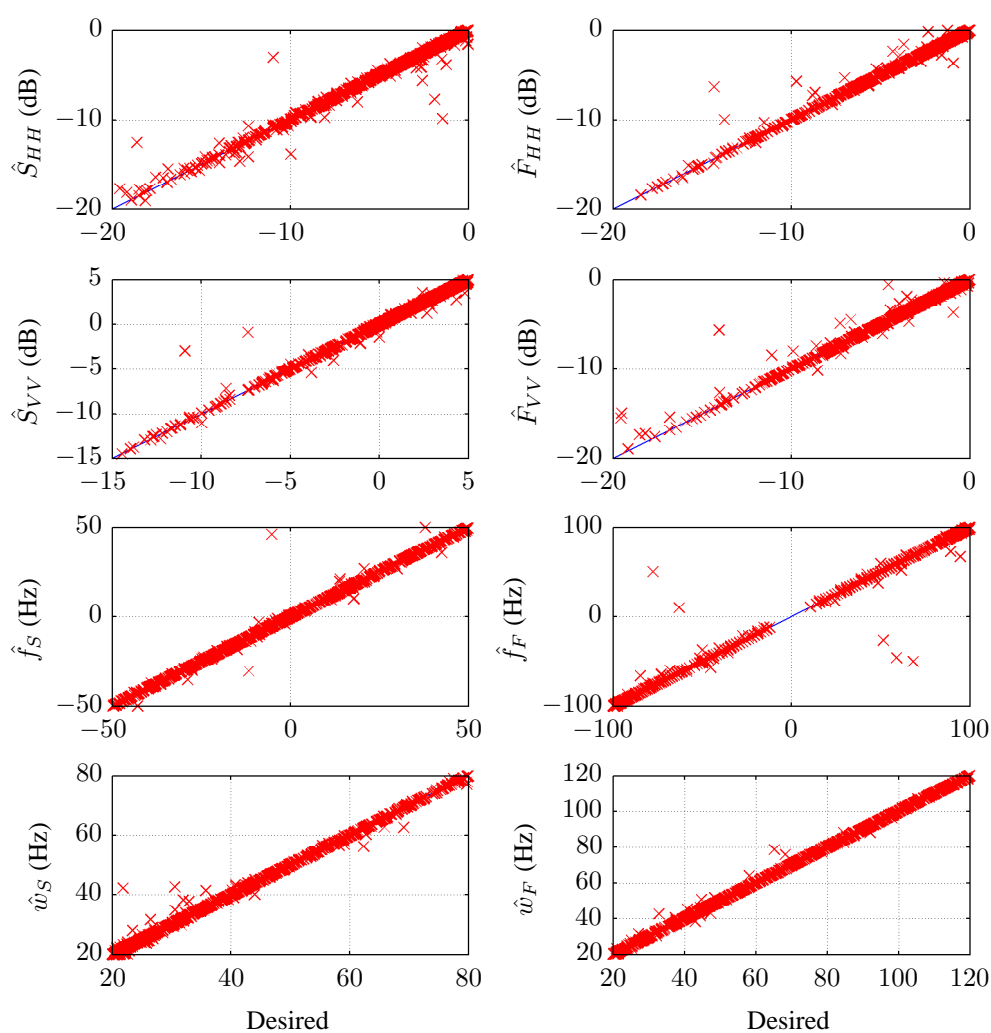
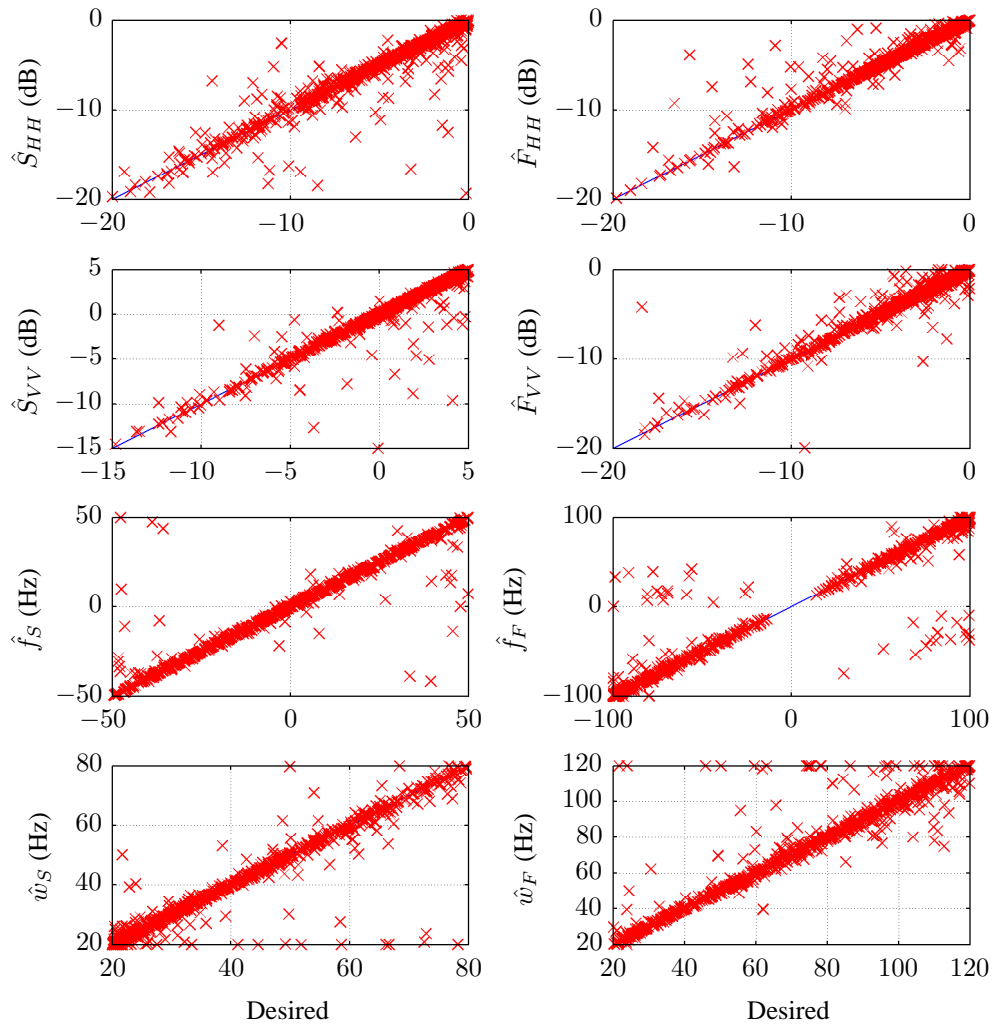
**Figure 30:** Goodness of fit scatter plot, dual-pol

Table 12: Full-pol parameter deviation error and correlation values

	S_{HH}	S_{VV}	f_S	w_S	F_{HH}	F_{VV}	f_F	w_F
Deviation (%)	7.43	3.84	3.22	4.83	3.84	5.45	4.83	7.05
Correlation	0.91	0.96	0.95	0.95	0.96	0.86	0.96	0.95

**Figure 31:** Goodness of fit scatter plot, full-pol

6 Sea-clutter analysis - two component model

This section provides an analysis of the two component underlying mean Doppler spectrum model for both the dual and full-pol data sets. For the dual-pol data, there is a nominal PRF of 600 Hz resulting in a complete un-aliased Doppler spectrum. Based on the simulation results in Section 5.3, this will provide the most accurate estimate of the model parameters. The data is collected over two consecutive runs and it is therefore assumed that the combined mean Doppler spectrum is representative of an equivalent full-pol system with a higher PRF. For the fully polarised data, there is a lower PRF which results in aliasing of the sea-clutter Doppler spectra. This will raise the edges of the spectrum as the aliased components wrap into the sampled frequencies. The parameter estimation problem is therefore more difficult as there are a number of parameter sets which can result from a good fit to the spread spectrum.

The first Section 6.1 presents model results for the dual-pol data set in the upwind and downwind directions. An analysis of the estimated model parameters in 5° increments over the azimuth direction is then presented in Section 6.2. The analysis is then repeated for the same full-pol data sets used in Section 4, except that now only the HH and VV polarisation channels are used for the underlying model. To avoid confusion, this data will be referred to as the co-polarised (co-pol) data. Section 6.3 presents examples of the model fit in the upwind and downwind directions and Section 6.4 looks at how the estimated model parameters vary over both azimuth and grazing angles.

6.1 Dual-pol Doppler spectrum

Two example range/Doppler images from the co-pol channels of the F9 dual-pol data set are shown in Figures 32-33. These cover the upwind and downwind directions respectively and are centred at 33° grazing. For both polarisation channels, a 2.8 s block of data has been used covering a 2° grazing angle region. In both images, there is clearly more than one scattering component present as can be seen by a series of waves on the right side for the upwind image and left side for the downwind image.

The upwind and downwind mean Doppler spectra are then shown in Figures 34-35 with the spread spectra on the left and underlying spectra on the right. The bi-modal nature of the mean Doppler spectrum can clearly be seen in both polarisation channels, particularly for the upwind direction. The estimated fit for the spread spectrum is very good with a NRMS error of less than 0.04 for each channel.

The underlying spectrum was constructed with the parameter estimates given in Table 13. The parameter estimates reveal that the slow HH component is 17 dB stronger in the upwind direction with little change for the fast HH component. There is little difference for the slow VV magnitude, while the fast VV magnitude is 2 dB greater in the upwind direction. For both wind directions, the slow VV magnitude is greater than the slow HH, while the fast VV magnitude is less than the fast HH. For the centre point, recall that the VV channel has been centred at the origin. Consequently, the estimated fits result in different signs for the slow and fast components with the slow centre points close to 0 Hz and the fast centre points roughly ± 45 Hz for the upwind and downwind directions respectively. For this comparison, the slow widths are similar, while the upwind fast width is 30 Hz greater than downwind.

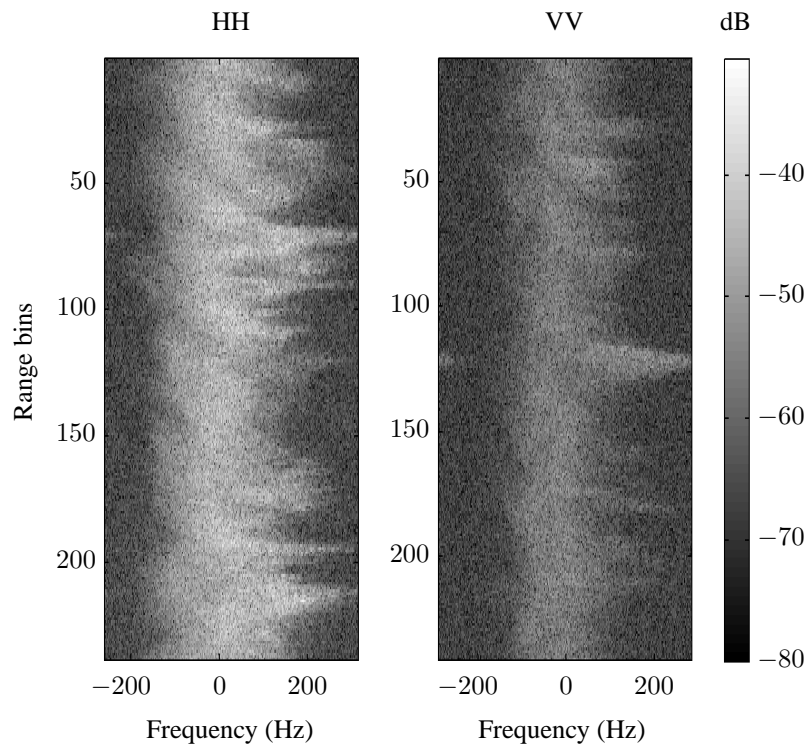


Figure 32: Dual-pol upwind range/Doppler sea-clutter image, co-pol channels only

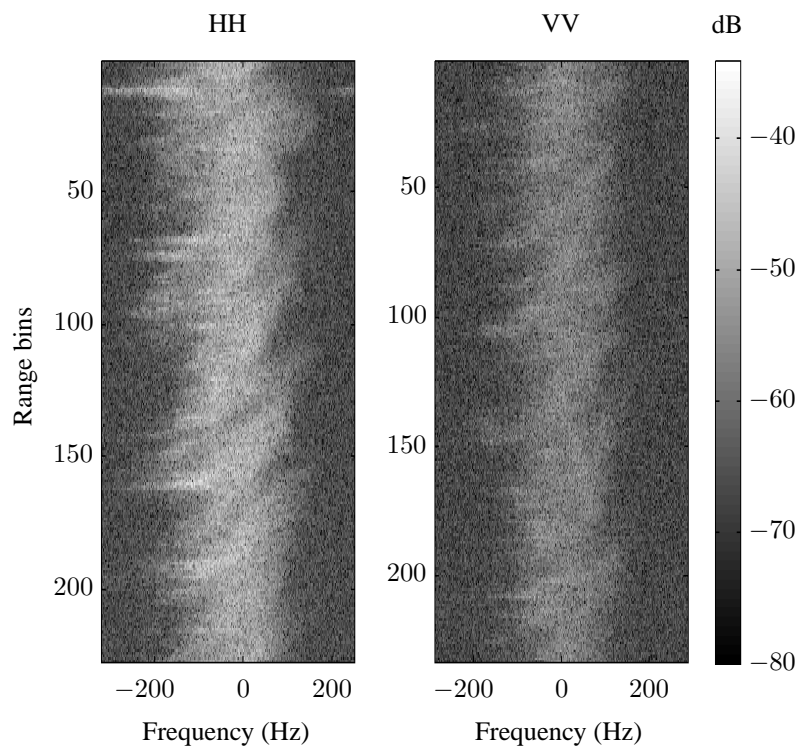


Figure 33: Dual-pol downwind range/Doppler sea-clutter image, co-pol channels only

Table 13: Dual-pol two component model parameters, magnitudes in dB, centre points and widths in Hz

	S_{HH}	S_{VV}	f_S	w_S	F_{HH}	F_{VV}	f_F	w_F
Upwind	-39.38	-35.24	-2.38	20.00	-46.28	-49.89	41.40	91.93
Downwind	-56.72	-36.72	4.93	24.63	-46.10	-52.05	-51.65	59.54

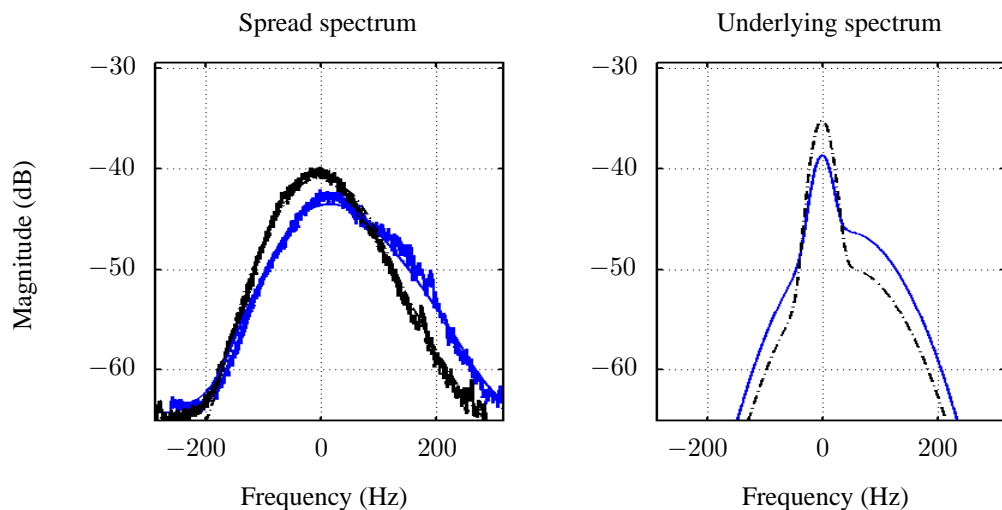


Figure 34: Dual-pol upwind mean Doppler spectrum, spread spectrum on left, estimated underlying spectrum on right, (—) HH, (.-) VV

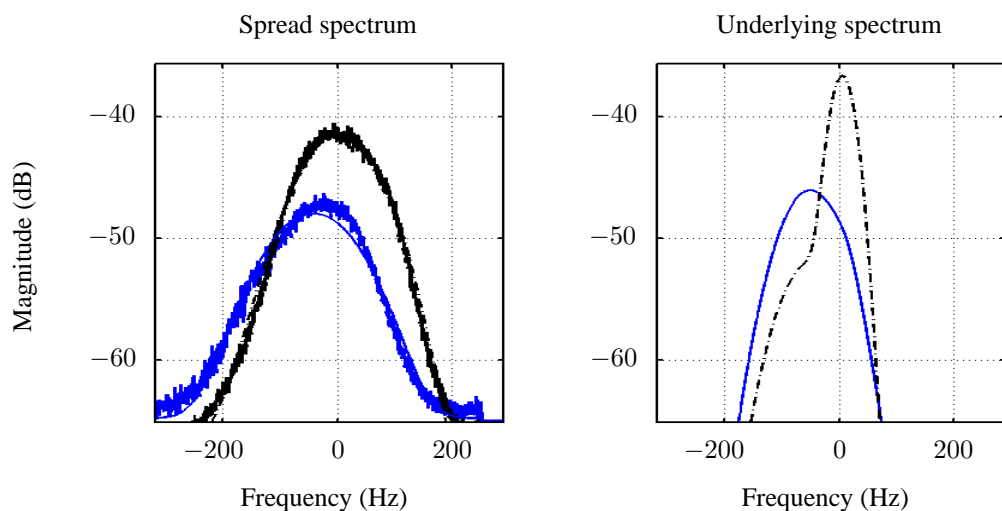


Figure 35: Dual-pol downwind mean Doppler spectrum, spread spectrum on left, estimated underlying spectrum on right, (—) HH, (.-) VV

6.2 Two component variation over azimuth - dual-pol

With the radar backscatter data collected along a circular flight path, the parameters were estimated for each 5° in azimuth, ϕ , with each of the data fits having a NRMS error between the measured and modelled spectra of less than 0.05. First inspection of the results reveal that some parameter estimates fluctuate due to the variability of sea-spikes over the observation time.

Figure 36 shows the variations in both the slow magnitudes S_{HH} and S_{VV} and fast magnitudes, F_{HH} and F_{VV} . For the slow magnitudes in the upwind region ($-90^\circ < \phi < 90^\circ$), the VV channel is 5-10 dB greater than the HH channel. A sinusoidal variation is observed for both channels with the maxima in the upwind and downwind directions and the minima in the cross wind directions. For the HH channel, there are significant fluctuations in the downwind region due to the variability of sea-spikes. For the fast magnitude, the HH return is nearly always greater than VV indicating the presence of dominant fast components in the HH channel.

The model centre points are shown on the left of Figure 37. The fast component varies sinusoidally around the upwind direction with its centre point reaching a maximum of 50 Hz. The slow centre point varies around 0 Hz with no discernable trend. The widths are shown on the right of this figure. The mean slow width fluctuates around 25 Hz with many points at the minimum allowable width of 20 Hz. For the fast width however, the average is around 100 Hz for the upwind region which reduces to 70 Hz at downwind.

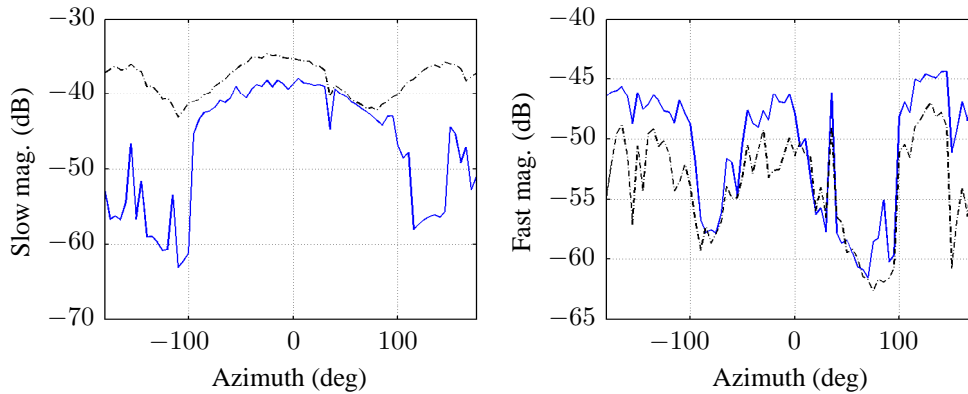


Figure 36: Dual-pol model magnitudes - slow on left, fast on right, (—) HH, (-.-) VV

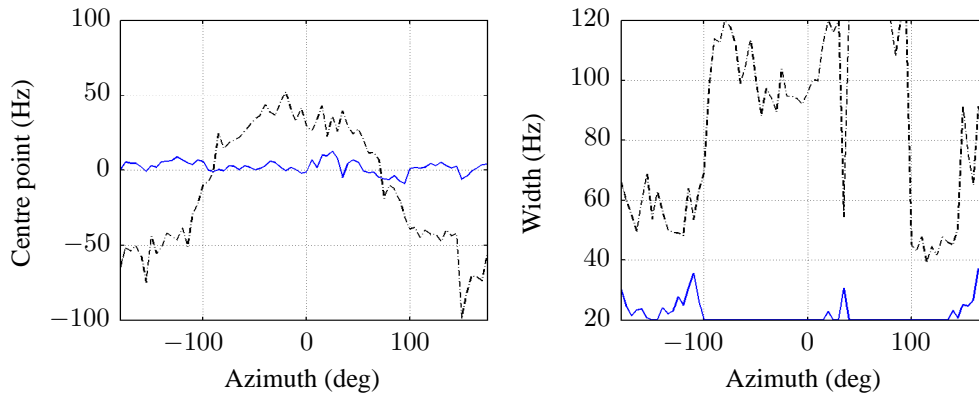


Figure 37: Dual-pol model centre points on left, widths on right, (—) slow, (-.-) fast

6.3 Co-pol Doppler spectrum

This section now repeats the analysis from Section 4.2 with the two component model for the underlying Doppler spectrum. The results are shown in Figures 38-39 with the spread spectra on the left and underlying spectra on the right. Although the bi-modal components are not as visible as in the dual-pol spread spectrum, the two component model still results in an excellent fit to the data with a NRMS error of less than 0.04 for each channel.

The underlying spectrum was constructed with the parameter estimates given in Table 14. They reveal that for the slow component, the upwind slow HH magnitude is approximately 6 dB greater than downwind, while for the VV channel, the downwind magnitude is 3 dB greater than upwind. For the fast component, there are only small differences between the wind directions for both polarisations. The slow centre points are close to 0 Hz with the fast centre points roughly ± 50 Hz for the two wind directions. For the slow width, the upwind value is 17 Hz greater than downwind, while the difference is reduced for the fast width.

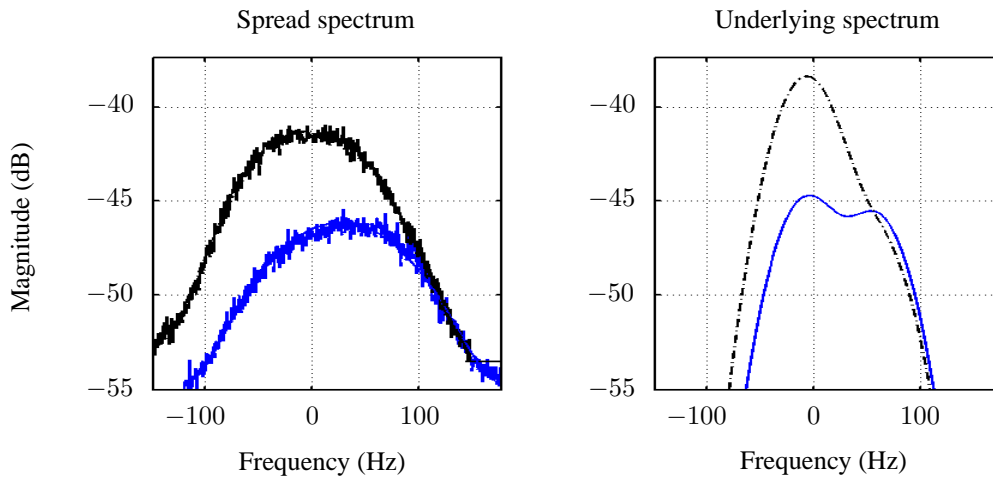


Figure 38: Co-pol upwind mean Doppler spectrum with two component, spread spectrum on left, estimated underlying spectrum on right, (—) HH, (---) VV

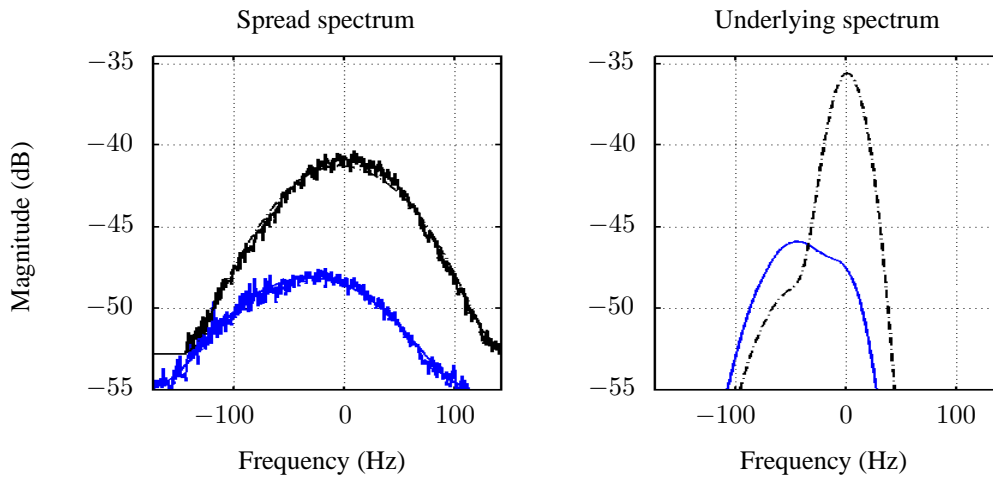


Figure 39: Co-pol downwind mean Doppler spectrum with two component, spread spectrum on left, estimated underlying spectrum on right, (—) HH, (---) VV

Table 14: Co-pol two component model parameters, magnitudes in dB, centre points and widths in Hz

	S_{HH}	S_{VV}	f_S	w_S	F_{HH}	F_{VV}	f_F	w_F
Upwind	-44.86	-38.41	-6.70	36.76	-45.80	-46.94	58.72	36.76
Downwind	-50.40	-35.63	0.78	20.00	-45.90	-48.90	-45.34	43.12

6.4 Two component variation over geometry - co-pol

By estimating the model parameters for each 5° in azimuth and 2° in grazing, a picture can be built up of how the model parameters change with geometry. Figures 40-41 shows the slow and fast magnitudes, S_{HH} , S_{VV} and F_{HH} , F_{VV} for the F35 data set. The slow HH and fast VV results fluctuate significantly due to the variability of sea-spikes over the observation time. However, the sinusoidal trend across azimuth is still present with a maximum in the upwind direction and increasing magnitude as the grazing increases. For the other two magnitudes, the fluctuations are not present and these trends become clearer. Between the slow VV and fast VV magnitudes, the change of magnitude over grazing is more pronounced. Also, for the slow component, the VV magnitude is approximately 10 dB larger than the HH channel, while for the fast component, the magnitudes are very similar between polarisation channels.

The model centre points, f_S , f_F are shown in Figure 42. A weak sinusoidal variation is present for the slow component which fluctuates by ± 20 Hz between the downwind and upwind directions with little change over grazing angle. The trend is reversed for the fast component with a maximum in the upwind direction of 100 Hz. Note that this variation of the slow centre point does not have a physical justification and is due to the combination of the arbitrary zero frequency and the method of model fitting. For both components, there is a trend with decreasing centre point as the grazing increases. The width results, w_S , w_F are then shown in Figure 43. There is no discernable trend for either component. The width means are 33 Hz for the slow component and 56 Hz for the fast component.

The second set of results for the F9 data set are shown in Figures 44-47 and have similar trends to F35. For the slow HH magnitude in Figure 44, there is now less fluctuation in the parameter estimates. For the fast magnitude results in Figure 45, there are regions where the fast HH magnitude is greater than VV, indicating where the non-Bragg scattering is more dominant. For the spectral width results in Figure 47, there is a slight trend in the fast component with increasing width in the upwind region between 15° - 30° grazing. The width means are 27 Hz for the slow component and 52 Hz for the fast component.

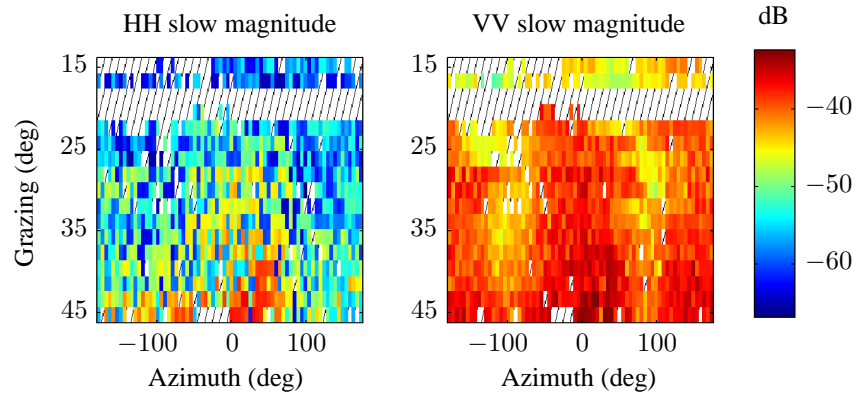


Figure 40: Two component model fit for F35, slow magnitude, left: HH, right: VV. Hashed areas indicate regions with poor or missing data.

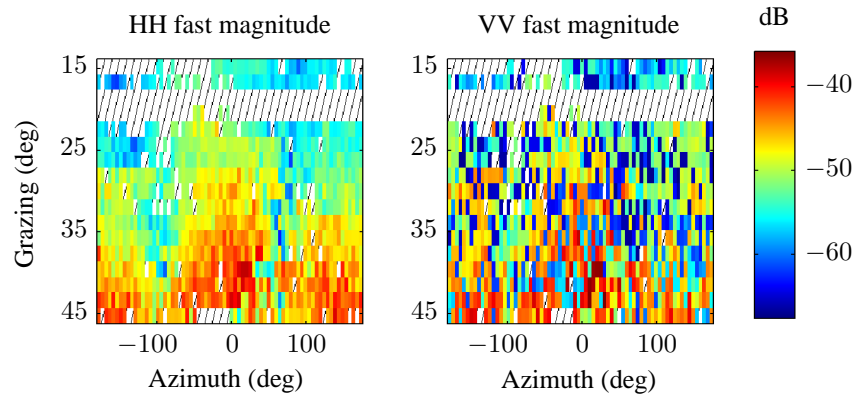


Figure 41: Two component model fit for F35, fast magnitude, left: HH, right: VV. Hashed areas indicate regions with poor or missing data.

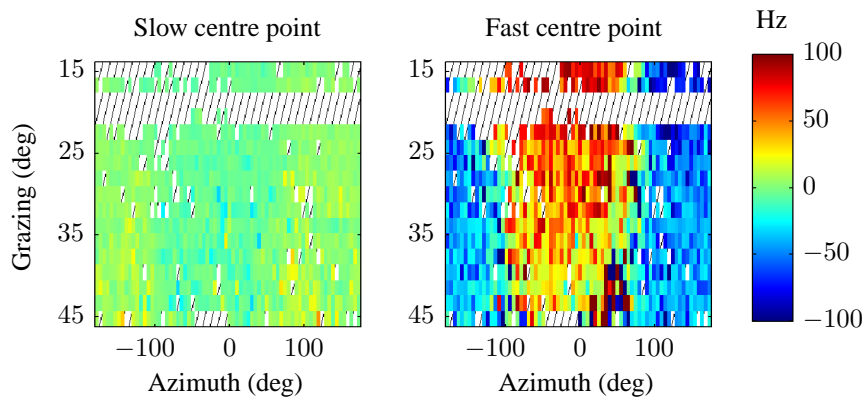


Figure 42: Two component model fit for F35, centre point, left: slow, right: fast. Note that the VV channel is shifted to have a Doppler centroid of 0 Hz with the HH channel shifted relatively. Hashed areas indicate regions with poor or missing data.

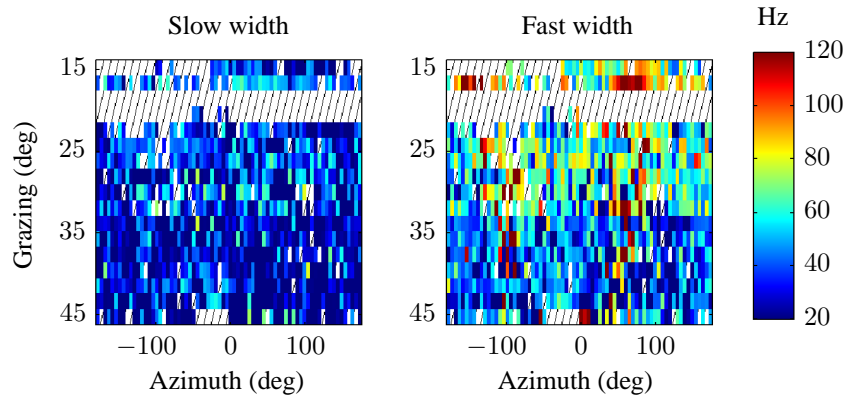


Figure 43: Two component model fit for F35, width, left: slow, right: fast. Hashed areas indicate regions with poor or missing data.

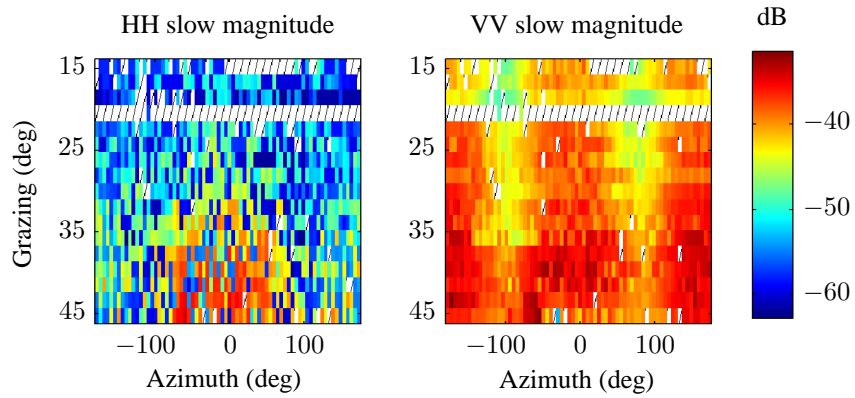


Figure 44: Two component model fit for F9, slow magnitude, left: HH, right: VV. Hashed areas indicate regions with poor or missing data.

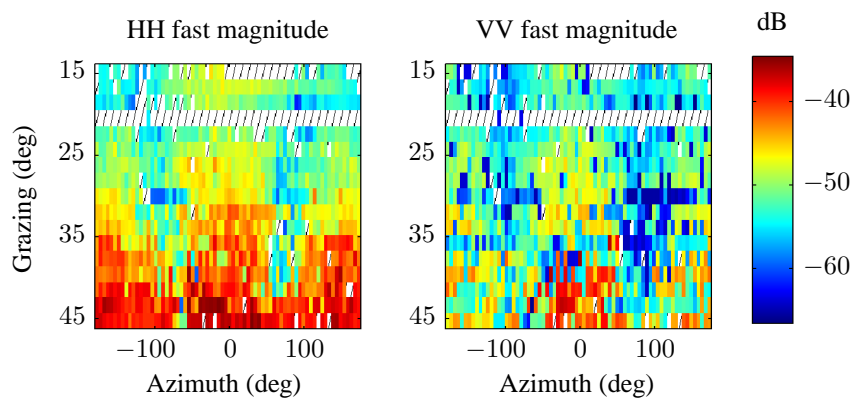


Figure 45: Two component model fit for F9, fast magnitude, left: HH, right: VV. Hashed areas indicate regions with poor or missing data.

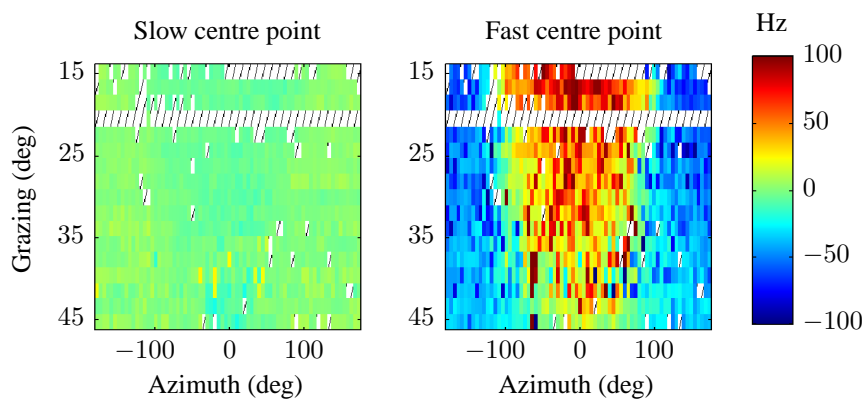


Figure 46: Two component model fit for F9, centre point, left: slow, right: fast. Note that the VV channel is shifted to have a Doppler centroid of 0 Hz with the HH channel shifted relatively. Hashed areas indicate regions with poor or missing data.

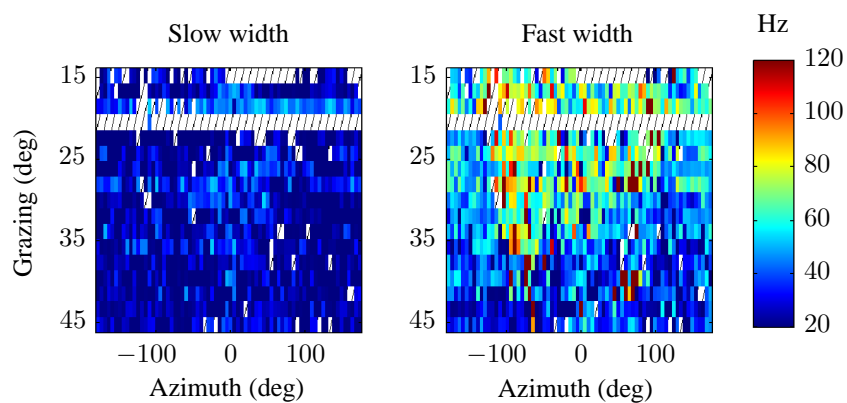


Figure 47: Two component model fit for F9, width, left: slow, right: fast. Hashed areas indicate regions with poor or missing data.

7 Temporal correlation

In this final section, the temporal correlation is analysed for both the one and two component underlying Doppler spectrum models. The autocorrelation function (ACF) is related to the mean Doppler spectrum through a Fourier transform and will in general be complex. The temporal decorrelation time is measured at the point where the absolute value of the ACF decays to $1/e$. If this single parameter is used to characterise the ACF (i.e. through a negative exponential model), the true Doppler spectrum cannot be recreated and it is approximated as symmetric and centred at 0 Hz. While the full Doppler spectrum is important for characterising and simulating sea-clutter, the temporal decorrelation time is commonly used to quantify the level of temporal correlation present in sea-clutter.

The next Section 7.1 demonstrate the relationship between the Doppler spectrum and temporal correlation, while Section 7.2 introduces a new model for the temporal decorrelation time as a function of wind speed and wave height.

7.1 Relationship between Doppler spectrum and temporal correlation

As stated above, the ACF is related to the mean Doppler spectrum through a Fourier transform. Figure 48 shows an example with the underlying Doppler spectrum on the left and the ACF on the right. For this example, the temporal decorrelation time is measured as 3.78 ms.

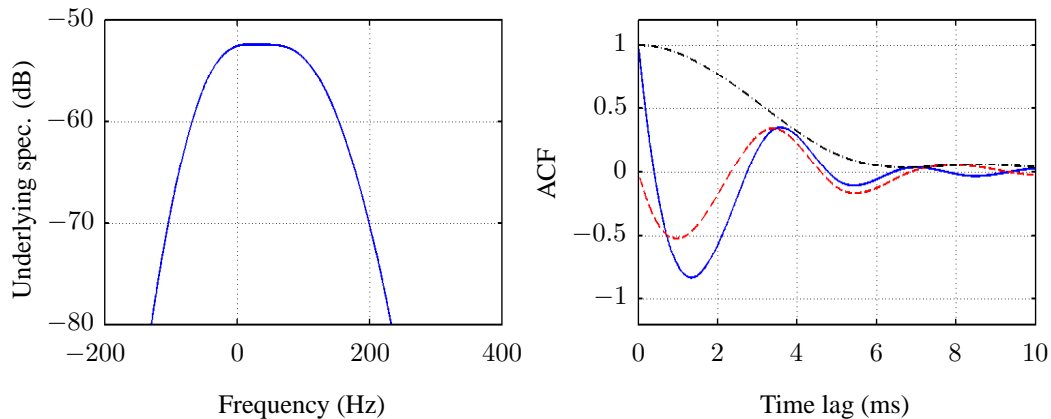


Figure 48: Autocorrelation example: left - underlying Doppler spectrum, right - normalised ACF (—) real, (--) imaginary, (-.-) absolute

The temporal decorrelation times for both underlying models are now presented in Figures 49-50 for the F35 data set and Figures 51-52 for the F9 data set. Only the co-pol channels are used with the same scale for comparison. In these results, the VV channel has a slightly longer decorrelation time, with no obvious trends due to the changes in geometry. For the F35 data set, the mean decorrelation times using the single component model are 6.21 and 7.57 ms for the HH and VV channels respectively. The two component model results are very similar with 6.87 and 9.99 ms. For the F9 data set, the mean decorrelation times using the single component model are 6.83 and 9.25 ms and for the two component model are 7.37 and 11.84 ms.

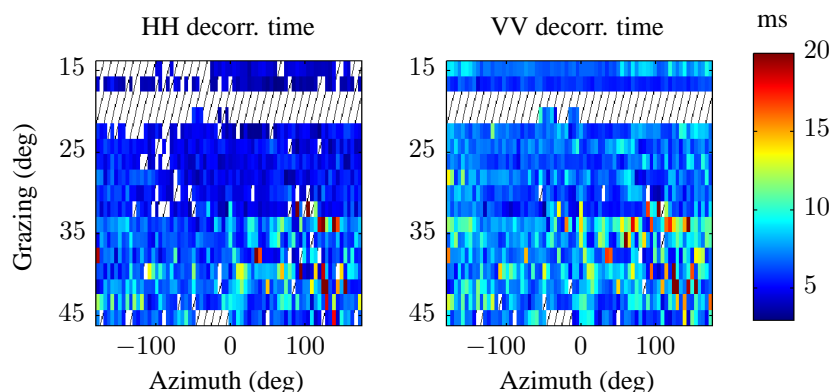


Figure 49: Temporal decorrelation time for F35 using single component model, left: HH, right: VV. Hashed areas indicate regions with poor or missing data.

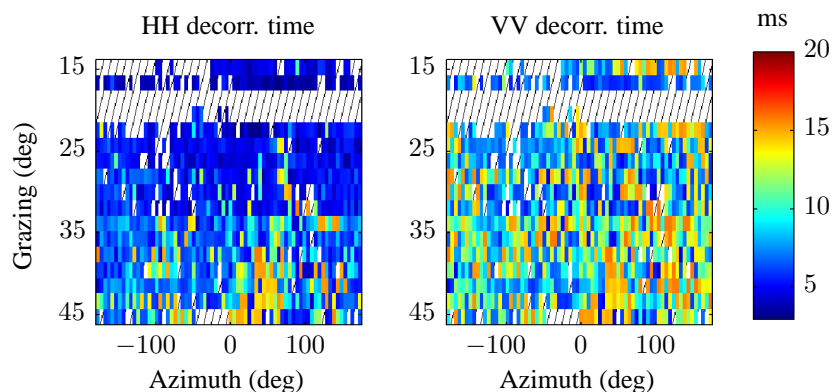


Figure 50: Temporal decorrelation time for F35 using two component model, left: HH, right: VV. Hashed areas indicate regions with poor or missing data.

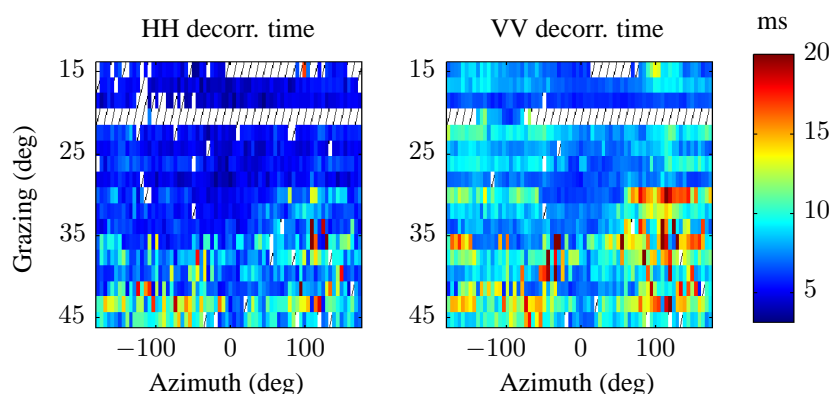


Figure 51: Temporal decorrelation time for F9 using single component model, left: HH, right: VV. Hashed areas indicate regions with poor or missing data.

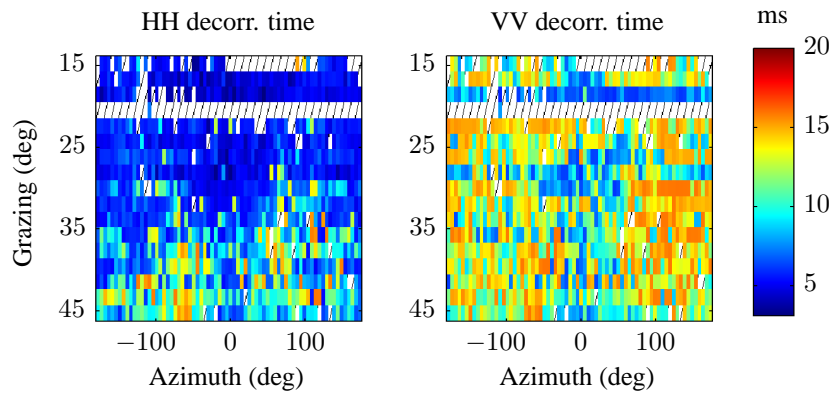


Figure 52: Temporal decorrelation time for F9 using two component model, left: HH, right: VV. Hashed areas indicate regions with poor or missing data.

7.2 Temporal decorrelation model

Results from the previous section demonstrated that there are no consistent trends in azimuth and grazing angle for the temporal decorrelation time. However, as shown in Section 4.4, the mean width can be related to wind speed and wave height. As a result of the relationship between the spectral width and temporal correlation, a similar model is now proposed for the mean temporal decorrelation time for the HH and VV polarisation channels. The model from Equation 25 is used with the temporal decorrelation time of the two component fit replacing the spectral width and the model coefficients given in Table 15.

Figures 53-54 show the model fit for the two component model where the trend is that the mean decorrelation times are longer when the wind speed and wave height are smaller. The RMS errors for the HH and VV channels are 1.1 and 0.74 ms respectively.

Table 15: Temporal decorrelation model parameters

	HH	VV
a_0	16.67	17.13
a_1	-0.69	-0.40
a_2	-0.87	-0.91

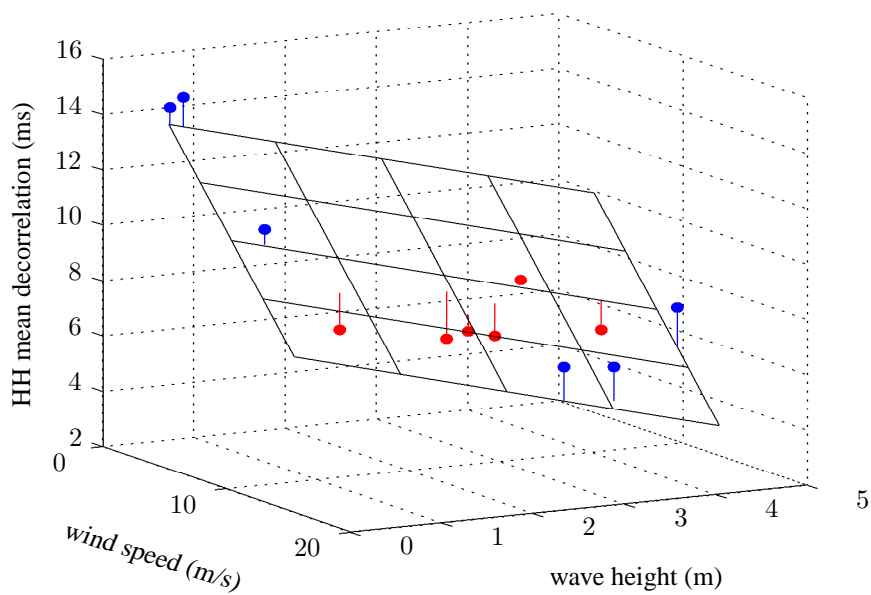


Figure 53: HH mean temporal decorrelation as a function of wind speed and wave height

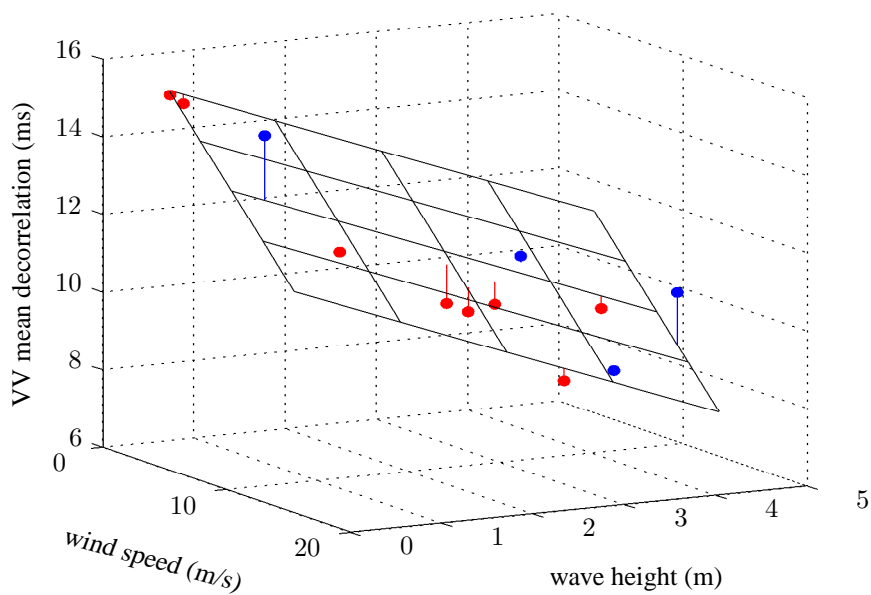


Figure 54: VV mean temporal decorrelation as a function of wind speed and wave height

8 Conclusion

Understanding the Doppler spectra of radar backscatter from the high grazing angle region of the sea is important for increasing our understanding of the underlying phenomenology, and through its relationship with the temporal correlation, can improve the fidelity of radar performance modelling in the maritime environment. The majority of studies of the Doppler spectra have been conducted at low grazing angles with a reasonably high PRF to completely capture all the components of the spectra. The data sets collected by the Ingara radar however were from a moving platform and resulted in a broadening of the radar beam. In addition, motion of the aircraft resulted in an unknown zero Doppler reference point and the low PRF which was used for the full-pol data collects resulted in aliasing of the spectra. Each of these ‘measurement’ effects with the addition of thermal noise are accounted for in the Doppler spectrum model.

The first analysis section considered a single Gaussian component as a model for the underlying Doppler spectra. This is the chosen model used in many previous studies on sea-clutter and is useful for baselining the new model against and comparing with results from the literature. The fully polarised data sets were used for this analysis which span 360° in azimuth and $15^\circ - 45^\circ$ in grazing. Determining the model parameters involved data fitting with an estimate of the underlying spectra convolved with the azimuth beam pattern and the addition of thermal noise. The spread spectrum is then compared with the data and the underlying model parameters modified according to an appropriate cost function. Characterisation of the model parameters is performed over a range of wind speeds and azimuth and grazing angles. There was a good match between the model magnitudes and the mean backscatter, with trends indicating a sinusoidal variation in azimuth with peaks in the upwind and downwind directions, while the grazing is approximately linear with increasing magnitude as grazing increased. The values for the centre points showed a peak for the HH channel when the grazing angle is small, which then decreased as the grazing increased. The upwind direction is largest along azimuth, with the downwind direction being strongly negative and a slight narrowing of the positive component observed as grazing increased. The spectral width was quite random over all azimuth and grazing angles with the HH width more closely resembling the VV width at higher grazing angles. When considering the sea conditions however, a good trend was observed with the mean width increasing as a function of wind speed and wave height.

A more suitable model for the high grazing region was then proposed to characterise the Doppler spectrum with two components representing the slow Bragg and the fast non-Bragg scattering. The design of the model accounts for the reduced Brewster angle damping above 20° grazing and allows both polarisation channels to receive the persistent whitecap and discrete sea-spike components, albeit with a different magnitude. The fitting accuracy of this model was then verified with simulated data using parameters to represent both the dual and full-pol data sets with radar measurement effects included for realism.

The two component model was then tested with both data sets. The dual-pol data was collected over two consecutive runs and it was assumed that the combined mean Doppler spectrum was representative of an equivalent full-pol system with a higher PRF. The data set spanned a small range of grazing angles, but covered the full 360° in azimuth. The bi-modal nature was clearly observed in both the spread and underlying Doppler spectra with the higher PRF allowing for a complete un-aliased Doppler spectrum and hence greater confidence in the parameter estimation. The estimated model magnitude parameters revealed that the VV channel is 5-10 dB greater than

the HH channel. A sinusoidal variation was observed for both channels with maxima in the upwind and downwind directions and minima in the cross wind directions. For the fast magnitude, the HH return was always greater than the VV indicating the presence of dominant fast components in the HH channel. Both model centre points were found to vary sinusoidally around the upwind direction and there was no discernable trend for the width parameters over azimuth.

Fitting the two component model to the co-pol channels of the full-pol data sets was a more difficult estimation problem as the lower PRF resulted in aliasing of the Doppler spectra. The two component model however, demonstrated an excellent fit to the data even though the bi-modal components were not as visible in the spread spectrum as for the dual-pol data set. Both the slow and fast magnitude components showed a reasonable match with a sinusoidal variation over azimuth, which increased as grazing increased. For the fast magnitudes, the relative levels were very similar with some sections where HH was greater than VV indicating where the non-Bragg scattering was more dominant. The model centre points demonstrated the sinusoidal variation with the slow component having a minimum in the upwind direction, while the fast component had a maximum. There was also a trend observed with decreasing centre point value as the grazing increased, which was more pronounced for the fast component. For the widths, there was no discernable trend with the slow component, while there was a minor trend observed for the fast component with decreasing width as the grazing increases.

The temporal decorrelation time is a metric commonly used in radar performance modelling for representing the level of temporal correlation present in the sea-clutter. The final contribution was to introduce a new model for this parameter as a function of wind speed and wave height.

Future work should involve the collection and analysis of full-pol data which is not aliased. A forward looking collection mode with a higher PRF would eliminate this and provide further insight into the validity of the proposed two component model. A separate study of the Doppler spectrum evolution along range and with shorter time scales is also planned for future work. In order to capture the geometric and sea state variations for use in parametric modelling, an empirical model could be constructed with a sinusoidal variation in azimuth, linear in grazing and a power-law for the wind speed. The temporal decorrelation model can also be used to improve the realism in radar performance studies.

Acknowledgements

The author would like to thank Dr. Yunhan Dong, Dr. Tom Winchester, Dr. Brett Haywood and Dr. Andrew Shaw for their review comments and the derivation in Appendix A.

References

- Bamler, R. & Runge, H. (1991) PRF-ambiguity resolving by wavelength diversity, *IEEE Transactions on Geoscience and Remote Sensing* **29**(6), 997–1003.
- Bass, F. G., Fuks, I. M., Kalmykov, A. I., Ostrovsky, I. E. & Rosenberg, A. D. (1968) Very high frequency radiowave scattering by a distributed sea surface, part II: scattering from an actual sea surface, *IEEE Transactions on Antennas and Propagation* **16**(5), 560–568.
- Crisp, D. J., Kyprianou, R., Rosenberg, L. & Stacy, N. J. (2008) Modelling X-band sea clutter at moderate grazing angles, in *IEEE International Radar Conference*, pp. 596–601.
- Crisp, D. J., Stacy, N. J. & Goh, A. S. (2006) *Ingara Medium-High Incidence Angle Polarimetric Sea Clutter Measurements and Analysis*, Technical Report DSTO-TR-1818, DSTO.
- Dong, Y. (2006) *Distribution of X-Band High Resolution and High Grazing Angle Sea Clutter*, Research Report DSTO-RR-0316, DSTO.
- Duncan, J. R., Keller, W. C. & Wright, J. W. (1974) Fetch and wind speed dependence of doppler spectra, *Radio Science* **9**, 809–819.
- Greco, M., Stinco, P. & Gini, F. (2010) Identification and analysis of sea radar clutter spikes, *IET Journal of Radar, Sonar and Navigation* **4**(2), 239–250.
- Guinard, N. W. & Daley, J. C. (1970) An experimental study of a sea clutter model, *Proceedings of the IEEE* **58**, 543–550.
- Hasselmann, K. & Schieler, M. (1970) Radar backscatter from the sea surface, in *Symposium on Naval Hydrodynamics*, pp. 361–388.
- Hicks, N. L., Knable, N., Kovaly, J. J., Newell, G. S., Ruina, J. P. & Sherwin, C. W. (1960) The spectrum of X-band radiation backscattered from the sea surface, *Journal of Geophysical Research* **65**(3), 825–837.
- Jessup, A. T., Keller, W. C. & Melville, W. K. (1990) Measurement of sea spikes in microwave backscatter at moderate incidence, *Journal of Geophysical Research* **95**(C6), 9679–9688.
- Jessup, A. T., Melville, W. K. & Keller, W. C. (1991a) Breaking waves affecting microwave backscatter, 1. detection and verification, *Journal of Geophysical Research* **96**(C11), 20,547–20,559.
- Jessup, A. T., Melville, W. K. & Keller, W. C. (1991b) Breaking waves affecting microwave backscatter, 2. dependence on wind and wave conditions, *Journal of Geophysical Research* **96**(C11), 20,561–20,569.
- Kalmykov, A. I. & Pustovoytenko, V. V. (1976) On polarization features of radio signals scattered from the sea surface at small grazing angles, *Journal of Geophysical Research* **81**(C12), 1960–1964.
- Keller, M. R., Gotwols, B. L. & Chapman, R. D. (2002) Multiple sea spike definitions: reducing the clutter, in *IEEE International Geoscience and Remote Sensing Symposium*, pp. 940–942.

- Kwoh, D. S. W. & Lake, B. M. (1983) The nature of microwave backscattering from water waves, in *NATO/AGARD Conference Proceedings*, pp. 23(1)–23(16).
- Lamont-Smith, T. (2004) Investigation of the variability of doppler spectra with radar frequency and grazing angle, *IEE Proceedings of Radar, Sonar and Navigation* **151**(5), 291–298.
- Lee, P. H. Y., Barter, J. D., Beach, K. L., Hindman, C. L., Lake, B. M., Rungaldier, H., Shelton, J. C., Williams, A. B., Yee, R. & Yuen, H. C. (1995a) X-band microwave backscattering from ocean waves, *Journal of Geophysical Research* **100**(C2), 2591–2611.
- Lee, P. H. Y., Barter, J. D., Caponi, E., Hidman, C. L., Lake, B. M. & Rungaldier, H. (1996) Wind-speed dependence of small-grazing-angle microwave backscatter from sea surfaces, *IEEE Transactions on Antennas and Propagation* **44**(3), 333–340.
- Lee, P. H. Y., Barter, J. D., Caponi, E., Hidman, C. L., Lake, B. M., Rungaldier, H. & Shelton, J. C. (1995b) Power spectral lineshapes of microwave radiation backscattered from sea surfaces at small grazing angles, *IEE Proceedings of Radar, Sonar and Navigation* **142**(5), 252–258.
- Lee, P. H. Y., Barter, J. D., Lake, B. M. & Thompson, H. R. (1998) Lineshape analysis of breaking-wave doppler spectra, *IEE Proceedings of Radar, Sonar and Navigation* **145**(2), 135–139.
- Lewis, R. L. & Olin, I. D. (1980) Experimental study and theoretical model of high resolution backscatter from the sea-clutter, *Radio Science* **15**, 815–826.
- Long, M. W. (2001) *Radar Reflectivity of Land and Sea - Third Edition*, Artech House.
- Lyzenga, D. R., Maffett, A. L. & Shuchman, R. A. (1983) The contribution of wedge scattering to the radar cross section of the ocean surface, *IEEE Transactions of Geoscience and Remote Sensing* **GE-21**(4), 502–505.
- Melief, H. W., Greidanus, H., van Genderen, P. & Hoogeboom, P. (2006) Analysis of sea spikes in radar sea clutter data, *IEEE Transactions on Geoscience and Remote Sensing* **44**(4), 985–993.
- Melville, W. K., Rozenberg, A. D. & Quigley, D. C. (1995) Laboratory study of polarized microwave scattering at grazing incidence, in *IEEE International Geoscience and Remote Sensing Symposium*, pp. 951–953.
- Nathanson, F. E., Reilly, J. P. & Cohen, M. N. (1991) *Radar Design Principles*, second edn, McGraw-Hill.
- Parfitt, A. & Nikolic, N. (2001) A dual-polarised wideband planar array for X-band synthetic aperture radar, in *IEEE Antennas and Propagation Society International Symposium*, Vol. 2, pp. 464–467.
- Peake, W. H. (1959) Theory of radar return from terrain, in *IRE Convention Record*, pp. 27–41.
- Pidgeon, V. W. (1968) Doppler dependence of radar sea return, *Journal of Geophysical Research* **73**(4), 1333–1341.
- Plant, W. J. (1997) A model for microwave Doppler sea return at high incidence angles: Bragg scattering from bound, tilted waves, *Journal of Geophysical Research* **102**(C9), 21,131–21,146.

- Quegan, S. (1994) Unified algorithm for phase and cross-talk calibration of polarimetric data: Theory and observations, *IEEE Transactions on Geoscience and Remote Sensing* **32**(1), 89–99.
- Rice, D. O. (1951) Reflections of electromagnetic waves from slightly rough surfaces, *Communications on Pure and Applied Maths* **4**, 361–378.
- Ritchie, M., Woodbridge, K. & Stove, A. G. (2010) Analysis of sea clutter distribution variation with Doppler using the compound K-distribution, in *IEEE Radarcon Conference*.
- Rosenberg, L. (2012a) The effect of temporal correlation with K and KK-distributed sea-clutter, in *IEEE Radarcon Conference*.
- Rosenberg, L. (2012b) Persistent sea-spike detection in medium grazing angle X-band sea-clutter, in *European SAR conference*, pp. 203–206.
- Rosenberg, L., Crisp, D. J. & Stacy, N. J. (2008) Characterisation of low-PRF X-band sea-clutter Doppler spectra, in *IEEE International Radar Conference*, pp. 100–105.
- Rosenberg, L., Crisp, D. J. & Stacy, N. J. (2010) Analysis of the KK-distribution with medium grazing angle sea-clutter, *IET Proceedings of Radar Sonar and Navigation* **4**(2), 209–222.
- Rosenberg, L. & Stacy, N. J. (2008) Analysis of medium angle X-band sea-clutter Doppler spectra, in *IEEE Radarcon Conference*.
- Rozenberg, A. D., Quigley, D. C. & Melville, W. K. (1996) Laboratory study of polarized scattering by surface waves at grazing incidence: The influence of long waves, *IEEE Transactions on Geoscience and Remote Sensing* **34**(6), 1331–1342.
- Rozenberg, A., Quigley, D., Ritter, M. & Melville, W. K. (1997) Laboratory study of polarized microwave scattering from steep waves at grazing incidence, in *IEEE International Geoscience and Remote Sensing Symposium*, pp. 711–713.
- Skolnik, M. I., ed. (2008) *Radar Handbook*, third edn, McGraw-Hill.
- Sletten, M. A., Trizna, D. B. & Hansen, J. P. (1996) Ultrawide-band radar observations of multipath propagation over the sea surface, *IEEE Transactions on Antennas and Propagation* **44**(5), 646–651.
- Stacy, N. J. S., Badger, D. P., Goh, A. S., Preiss, M. & Williams, M. L. (2003) The DSTO Ingara airborne X-band SAR polarimetric upgrade: first results, in *IEEE International Geoscience and Remote Sensing Symposium*, Vol. 7, pp. 4474 – 4476.
- Trizna, D. B. (1997) A model for Brewster angle damping and multipath effects on the microwave radar sea echo at low grazing angles, *IEEE Transactions on Geoscience and Remote Sensing* **35**(5), 1232–1244.
- Valenzuela, G. R. & Laing, M. B. (1970) Study of Doppler spectra of radar sea echo, *Journal of Geophysical Research* **75**, 551–563.
- Valenzuela, G. R., Laing, M. B. & Daley, J. C. (1971) Ocean spectra for the high-frequency waves as determined from airborne radar measurements, *Journal of Marine Research* **29**, 69–84.

- Walker, D. (2000) Experimentally motivated model for low grazing angle radar doppler spectra of the sea surface at small grazing angles, *IEE Proceedings of Radar, Sonar and Navigation* **147**(3), 114–121.
- Walker, D. (2001a) Doppler modelling of radar sea clutter, *IEE Proceedings of Radar, Sonar and Navigation* **148**(2), 73–80.
- Walker, D. (2001b) *Model and Characterisation of Radar Sea Clutter*, PhD thesis, University College London.
- Ward, K. D., Tough, R. J. A. & Watts, S. (2006) *Sea Clutter: Scattering, the K-Distribution and Radar Performance*, The Institute of Engineering Technology.
- Watts, S. (2012) Modeling and simulation of coherent sea clutter, *IEEE Transaction on Aerospace and Electronic Systems* **48**(4), 3303–3317.
- Werle, B. O. (1995) Sea backscatter, spikes and wave group observations at low grazing angles, in *IEEE International Radar Conference*, pp. 187–195.
- Wright, J. W. (1966) Backscattering from capillary waves with application to sea clutter, *IEEE Transactions on Antennas and Propagation* **AP-14**(6), 749–754.
- Wright, J. W. (1968) A new model for sea clutter, *IEEE Transactions on Antennas and Propagation* **16**(2), 217–223.

Appendix A Doppler spectrum convolution derivation

This appendix derives the relationship between the power spectral density of the stationary and moving scatterers in a scene and the azimuth antenna beampattern. The received signal model after motion compensation was given in Equation 6 as a function of spatial frequencies k_x, k_y . The next stage in pre-processing is to compensate for the elevation beampattern and hence the measured antenna two-way beampattern, $a(\cdot)$ can be written solely as a function of azimuth. The signal can then be written as

$$X(k_x, k_y) = \sum_l \sum_m \sqrt{a(y_m)} f(x_l, y_m) \exp[-jk_x(x_l - v_{x_l}\tau) - jk_y(y_m - v_{y_m}\tau)] \quad (\text{A1})$$

where each scatterer on the sea surface can be modelled with position (x_l, y_m) and velocity (v_{x_l}, v_{y_m}) components with the indices (l, m) relating the position index in the slant-range and azimuth directions. Also, in this model, $f(\cdot)$ is the radar backscatter, and τ is the pulse repetition interval. The power spectral density is given by

$$\begin{aligned} P_0(k_x, k_y) &= E \{X(k_x, k_y)X^*(k_x, k_y)\} \\ &= E \left\{ \sum_{l'} \sum_{m'} \sum_{l''} \sum_{m''} \sqrt{a(y_{m'})} f(x_{l'}, y_{m'}) \exp[-jk_x(x_{l'} - v_{x_{l'}}\tau) - jk_y(y_{m'} - v_{y_{m'}}\tau)] \right. \\ &\quad \times \left. \sqrt{a(y_{m''})} f^*(x_{l''}, y_{m''}) \exp[jk_x(x_{l''} - v_{x_{l''}}\tau) + jk_y(y_{m''} - v_{y_{m''}}\tau)] \right\} \\ &= \sum_{l'} \sum_{m'} \sum_{l''} \sum_{m''} \sqrt{a(y_{m'})} \sqrt{a(y_{m''})} E \{f(x_{l'}, y_{m'}) f^*(x_{l''}, y_{m''})\} \\ &\quad \times \exp[-jk_x(x_{l'} - v_{x_{l'}}\tau - (x_{l''} - v_{x_{l''}}\tau)) - jk_y(y_{m'} - v_{y_{m'}}\tau - (y_{m''} - v_{y_{m''}}\tau))] \end{aligned} \quad (\text{A2})$$

Now by assuming that each return from the radar backscatter is independent, the four summations become two and the expectation in Equation A2 can be simplified by

$$\begin{aligned} E \{f(x_{l'}, y_{m'}) f^*(x_{l''}, y_{m''})\} &\Rightarrow E \{f(x_l, y_m) f^*(x_l, y_m)\} \\ &= E \{|f(x_l, y_m)|^2\} \end{aligned} \quad (\text{A3})$$

where $l = l' = l''$ and $m = m' = m''$. Then by applying Parseval's formula in the azimuth spatial domain, Equation A2 can be written as

$$\begin{aligned} P_0(k_x, k_y) &= \mathcal{F} \{a(y_m) | y_m\} \otimes_{k_y} \mathcal{F} \{E \{|f(x_l, y_m)|^2\} | x_l, y_m\} \\ &= A(k_y) \otimes_{k_y} \Psi(k_x, k_y) \end{aligned} \quad (\text{A4})$$

where $A(k_y)$ antenna beampattern in the azimuth spatial frequency domain, and $\Psi(k_x, k_y)$ is the underlying mean Doppler spectrum of the stationary and moving scatterers. The power spectral density can then be written solely in terms of the Doppler frequency, f , by a transformation of variables $k_y = 4\pi f/c$ where c is the speed of light,

$$P_0(f) = A(f) \otimes_f \Psi(f). \quad (\text{A5})$$

Appendix B Convolution of two Gaussians

This appendix derives the convolution of two Gaussians, $b(f)$ and $w(f)$

$$P(f) = b(f) \otimes w(f) \quad (\text{B1})$$

where

$$b(f) = a_1 \exp \left[-\frac{(f - \mu_1)^2}{\sigma_1^2} \right], \quad (\text{B2})$$

$$w(f) = a_2 \exp \left[-\frac{(f - \mu_2)^2}{\sigma_2^2} \right]. \quad (\text{B3})$$

The easiest solution is to take Fourier transforms of both components, multiply and then invert the Fourier transform. For the signal $b(f)$, the Fourier transform is given by

$$B(u) = a_1 \sigma_1 \sqrt{\pi} \exp \left[-\pi^2 u^2 \sigma_1^2 - j\pi u \mu_1 \right]. \quad (\text{B4})$$

The convolved output of Equation B1 then becomes

$$\begin{aligned} P(u) &= a_1 \sigma_1 \sqrt{\pi} \exp \left[-\pi^2 u^2 \sigma_1^2 - j\pi u \mu_1 \right] a_2 \sigma_2 \sqrt{\pi} \exp \left[-\pi^2 u^2 \sigma_2^2 - j\pi u \mu_2 \right] \\ &= a_1 a_2 \sigma_1 \sigma_2 \pi \exp \left[-\pi^2 u^2 (\sigma_1^2 + \sigma_2^2) - j\pi u (\mu_1 + \mu_2) \right] \end{aligned} \quad (\text{B5})$$

which can be written in the form of Equation B4

$$f(u) = a_3 \sqrt{\sigma_1^2 + \sigma_2^2} \sqrt{\pi} \exp \left[-\pi^2 u^2 (\sigma_1^2 + \sigma_2^2) - j\pi u (\mu_1 + \mu_2) \right] \quad (\text{B6})$$

where

$$a_3 = a_1 a_2 \frac{\sigma_1 \sigma_2}{\sqrt{\sigma_1^2 + \sigma_2^2}} \sqrt{\pi}. \quad (\text{B7})$$

This gives the form of the convolved output as

$$P(f) = a_1 a_2 \frac{\sigma_1 \sigma_2}{\sqrt{\sigma_1^2 + \sigma_2^2}} \sqrt{\pi} \exp \left[-\frac{(f - (\mu_1 + \mu_2))^2}{\sigma_1^2 + \sigma_2^2} \right]. \quad (\text{B8})$$

DEFENCE SCIENCE AND TECHNOLOGY ORGANISATION DOCUMENT CONTROL DATA				1. CAVEAT/PRIVACY MARKING	
2. TITLE Characterisation of High Grazing Angle X-band Sea-clutter Doppler Spectra			3. SECURITY CLASSIFICATION Document (U) Title (U) Abstract (U)		
4. AUTHOR Luke Rosenberg			5. CORPORATE AUTHOR Defence Science and Technology Organisation PO Box 1500 Edinburgh, South Australia 5111, Australia		
6a. DSTO NUMBER DSTO-RR-0397		6b. AR NUMBER 015-704		6c. TYPE OF REPORT Research Report	
7. DOCUMENT DATE August, 2013					
8. FILE NUMBER 2012/1171383/1	9. TASK NUMBER AIR7000	10. TASK SPONSOR DGAD	11. No. OF PAGES 58	12. No. OF REFS 55	
13. URL OF ELECTRONIC VERSION http://www.dsto.defence.gov.au/publications/scientific.php			14. RELEASE AUTHORITY Chief, National Security and ISR Division		
15. SECONDARY RELEASE STATEMENT OF THIS DOCUMENT <i>Approved for Public Release</i> <small>OVERSEAS ENQUIRIES OUTSIDE STATED LIMITATIONS SHOULD BE REFERRED THROUGH DOCUMENT EXCHANGE, PO BOX 1500, EDINBURGH, SOUTH AUSTRALIA 5111</small>					
16. DELIBERATE ANNOUNCEMENT No Limitations					
17. CITATION IN OTHER DOCUMENTS No Limitations					
18. DSTO RESEARCH LIBRARY THESAURUS Sea-clutter, Doppler spectrum, radar					
19. ABSTRACT Collection of radar sea-clutter for research purposes is typically performed from a clifftop looking out to sea as it is relatively simple and inexpensive. This constrains the radar look direction with respect to the wind and limits the grazing angle. To improve our understanding at high grazing angles in the range 15° to 45°, the DSTO's Ingara airborne X-band fully polarimetric radar has been used to collect 12 days worth of sea-clutter data. It has previously been shown that Walker's mean Doppler spectrum model is not suitable at these grazing angles and hence a new two component model is proposed which captures both the 'slow' Bragg component and the 'fast' non-Bragg component of the radar backscatter. A temporal decorrelation model is then presented which can be used to provide realistic performance prediction modelling.					